

# DYNAMICAL HOTNESS, STAR FORMATION QUENCHING AND GROWTH OF SUPERMASSIVE BLACK HOLES

HUI HONG<sup>1,2</sup>, HUIYUAN WANG<sup>1,2</sup>, H. J. MO<sup>3</sup>, ZIWEN ZHANG<sup>1,2</sup>, GUANGWEN CHEN<sup>1,2</sup>, WENTAO LUO<sup>1,2</sup>, TINGGUI WANG<sup>1,2</sup>,  
PENGFEI LI<sup>4</sup>, RENJIE LI<sup>1,2</sup>, YAO YAO<sup>1,2</sup>, AND AOXIANG JIANG<sup>1,2</sup>

*Draft version July 20, 2023*

## ABSTRACT

A stellar system is dynamically hot when its kinetic energy is dominated by random motion represented by the velocity dispersion  $\sigma_{hot}$ . We use MaNGA data to obtain inner and outer dispersion of a galaxy,  $\sigma_{in}$  and  $\sigma_{out}$ , to characterize its dynamical status and study its connection with star-formation quenching and the growth of supermassive black hole(SMBH). We divide galaxies into fully quenched (FQGs), partially quenched (PQGs) and fully star-forming (FSGs) populations, and identify quenched central cores (QCCs) in PQGs. The galaxy distribution in  $(\sigma_{in}/\sigma_{hot})$ - $(\sigma_{out}/\sigma_{hot})$  diagram is L-shaped, consisting of a horizontal sequence ( $\sigma_{out}/\sigma_{hot} \sim 0$ ) and a vertical sequence ( $\sigma_{in}/\sigma_{hot} \sim 1$ ). FQGs and QCCs are located at the top of the vertical sequence,  $\sigma_{out}/\sigma_{hot} \sim 1$ , and are thus dynamically hot over their entire bodies. PQGs reside along the vertical sequence, so they have hot center but cold outskirt. FSGs are diverse and can be found in both sequences. Galaxy structural properties, star formation and AGN activities make a transition along the horizontal sequence at  $\sigma_{in}/\sigma_{hot} \sim 0.5$ , and along the vertical sequence at  $\sigma_{out}/\sigma_{hot} \sim 0.5$ . The fractions of optical AGNs and barred galaxies increase rapidly in the first transition and decline rapidly in the second; radio galaxies are located at the top of the vertical sequence. Our results demonstrate that star formation quenching and SMBH growth are effective only in dynamically hot systems. A simple model along this line can reproduce the observed SMBH scaling relations. We discuss how secular processes and strong interactions can make a system dynamically hot, and lead to the SMBH growth and star-formation quenching.

*Subject headings:* galaxies: evolution – galaxies: kinematics and dynamics – galaxies: structure – methods: observational – methods: data analysis

## 1. INTRODUCTION

The quenching of star formation in galaxies is one of the key processes during the evolution of the galaxy population. Observations show that star formation quenching began quite early, at least at redshift  $z = 3$  (Muzzin et al. 2013; Straatman et al. 2014; Ilbert et al. 2013), and generated a population of galaxies that are distinct from the star-forming population in color, morphology, gas content, and large-scale clustering (e.g. Strateva et al. 2001; Baldry et al. 2004; Brinchmann et al. 2004; Zehavi et al. 2011; Fabello et al. 2011; Wang et al. 2018c). Thus, quenching seems to have played a key role in producing the rich diversity of the observed galaxy population. Theoretically, numerous hypotheses have been proposed to understand the underlying mechanisms for star formation quenching (see reviews in Mo et al. 2010; Fabian 2012; Heckman & Best 2014; Wechsler & Tinker 2018; Boselli et al. 2022).

Many internal properties of galaxies, such as stellar mass, morphology, bulge mass, central stellar surface density, and central velocity dispersion, are found to correlate with the quenching properties of galaxies (Baldry et al. 2004; Peng et al. 2010; Cheung et al. 2012; Fang et al. 2013; Bluck et al. 2014, 2016; Woo et al. 2015; Wang et al. 2018b; Chen et al. 2020a; Bluck et al. 2022). For example, quiescent (quenched) galaxies tend to be more massive and compact than star-forming galaxies, have denser stellar cores and higher central velocity dispersion. Such correlations are particularly prominent for central galaxies, which are the most massive ones in dark matter halos, presumably because central galaxies are less affected by environmental effects (e.g. Li et al. 2020). Recently, based on weak lensing and HI rotational curve data, it is revealed that massive disk galaxies have a very high baryon-to-star conversion efficiency (Posti et al. 2019; Zhang et al. 2022). It hints that star formation can not be quenched if morphological transformation does not happen. All of these suggest a connection between quenching and morphological transformation.

The internal properties of galaxies are correlated with each other. For example, the bulge-to-total mass ratio tends to increase with galaxy stellar mass,  $M_*$ , and the central stellar mass surface density is tightly correlated with the central velocity dispersion ( $\sigma_{in}$ ) (e.g. Fang et al. 2013; Saglia et al. 2016; Bluck et al. 2020a). Among

<sup>1</sup>Key Laboratory for Research in Galaxies and Cosmology, Department of Astronomy, University of Science and Technology of China, Hefei, Anhui 230026, China; js2011@mail.ustc.edu.cn, whywang@ustc.edu.cn

<sup>2</sup>School of Astronomy and Space Science, University of Science and Technology of China, Hefei 230026, China

<sup>3</sup>Department of Astronomy, University of Massachusetts, Amherst MA 01003-9305, USA

<sup>4</sup>Department of Physics and Astronomy, University of Utah, UT 84112, USA

them, the well-known relation is the Faber-Jackson relation for elliptical and early-type galaxies, a tight relation between stellar mass and central velocity dispersion:  $M_* \propto \sigma_{\text{in}}^{3\sim 4}$  (Faber & Jackson 1976; Gallazzi et al. 2006; Aquino-Ortiz et al. 2018; Oh et al. 2020). Thus, the observed correlation of quenching with internal properties alone does not provide causality between them.

One of the most studied parameters is the central stellar mass surface density within 1 kpc,  $\Sigma_1$  (e.g. Franx et al. 2008; Cheung et al. 2012; Fang et al. 2013; Barro et al. 2017; Ellison et al. 2018; Bluck et al. 2020a). Previous studies found that the fraction of quenched galaxies increases with  $\Sigma_1$ , particularly rapidly around  $\log \Sigma_1 / (M_\odot / \text{kpc}^2) \sim 9.5$  (e.g. Cheung et al. 2012). Along the same lines, Fang et al. (2013) found an L-shaped distribution of galaxies in  $\Sigma_1$ -color space, indicating a rapid transition from the star-forming (blue) to quiescent (red) populations at a characteristic value of  $\Sigma_1$ . Barro et al. (2017) extended the analysis to high redshift and found similar results. However, the central stellar mass surface density does not change monotonously with stellar mass for massive elliptical galaxies (e.g. Graham & Guzmán 2003). Moreover, Fang et al. (2013) found that quenched and star-forming galaxies have similar median stellar mass density profiles at large radii, even though the two populations have different morphology. It suggests that the quenching is not regulated by stellar mass surface density alone.

The stellar velocity dispersion,  $\sigma$ , is another quantity widely used to indicate the dynamic structure of a galaxy. For instance, dynamically cold stellar components, such as galaxy disks, usually have much lower velocity dispersion than dynamically hot components, such as bulges and elliptical galaxies (e.g. Brook et al. 2012; Cappellari 2016; Zhu et al. 2018; Du et al. 2020; Zhu et al. 2022b). Fang et al. (2013) found an L-shaped transition in the velocity dispersion-color diagram, similar to that seen in the  $\Sigma_1$ -color diagram. Bluck et al. (2020a, 2022) used a machine learning technique to analyze various correlations of quenching with other galaxy properties, and found that the central velocity dispersion,  $\sigma_{\text{in}}$ , is the most predictive parameter for star formation quenching (see also Wake et al. 2012). Furthermore, Brownson et al. (2022) found that the velocity dispersion performs better than other rotation-related dynamical parameters. Clearly, stellar velocity dispersion merits further investigation as a potentially key factor in driving galaxy quenching.

The mass of supermassive black hole (SMBH) in a galaxy is found to be tightly correlated with the velocity dispersion and mass of the spheroid component of the host galaxy (Magorrian et al. 1998; Ferrarese & Merritt 2000; Gebhardt et al. 2000; Aller & Richstone 2007; Graham 2008; Kormendy & Ho 2013; Saglia et al. 2016; Graham & Sahu 2023). These correlations are usually referred to as the SMBH scaling relations (BHSRs). The correlation of quenching properties with  $\sigma_{\text{in}}$  and  $\Sigma_1$  may thus be a consequence of feedback from active galactic nuclei (AGNs). Observationally, attempts have been made to find the best predictor of the SMBH mass ( $M_{\text{BH}}$ ) based on various combinations of velocity dispersion and spheroid mass,  $M_{\text{sph}}$  (Feoli & Mele 2005; Aller & Richstone 2007; Hopkins et al. 2007b; Soker & Meiron 2011;

Mancini & Feoli 2012). More recently, Graham & Sahu (2023) found that the  $M_{\text{BH}}-M_{\text{sph}}$  scaling relation for elliptical galaxies has a significant offset relative to that for bulges in other early-type and spiral galaxies (see also Bogdán et al. 2018; Sahu et al. 2019). This hints that the BHSRs in bulges and elliptical galaxies may not share the same origin. However, caution needs to be exercised before drawing such a conclusion. Indeed, simulations and observational data show that, in addition to bulges, galaxies contain other dynamically hot components such as inner stellar halos discovered in nearby galaxies (see Brook et al. 2012; Ibata et al. 2014; Du et al. 2020; Zhu et al. 2022a,b), which may also be related to the formation of SMBHs. Clearly, more investigations are needed, in particular to understand the BHSRs from the perspective of galaxy quenching.

A great deal of theoretical work has been devoted to modeling the AGN feedback, including analytic and empirical models (e.g. Silk & Rees 1998; Fabian 1999; Chen et al. 2020b), semi-analytic models (e.g. Croton et al. 2006; Bower et al. 2006), and hydro-dynamical simulations (e.g. Di Matteo et al. 2005; Hopkins et al. 2007a; Schaye et al. 2015; Dubois et al. 2016; Pillepich et al. 2018; Davé et al. 2019). Many of the mechanisms proposed are relevant not only to SMBH and AGN formation (Di Matteo et al. 2005; Hopkins & Quataert 2011), but can also change the structure of the host galaxy, thus predicting some correlations of SMBHs (and their feedback) with the structure of host galaxies. Broadly, the mechanisms can be divided into two categories: rapid and secular (Kormendy & Kennicutt 2004). Major mergers of galaxies, which belong to the first category, can scramble galaxy disks and trigger starbursts, produce a dynamically hot stellar system, such as a bulge or an elliptical. Bar-driven processes, which belong to the second category, can also rearrange stars and gaseous clouds in a galaxy. In particular, bars can drive gas into the center of a galaxy and cause the buildup of a central concentration resembling a dynamically hot compact object. Interactions with neighboring galaxies and minor mergers may also play a role by pumping energy into a galaxy disk, making it dynamically hotter. These mechanisms can thus help us to understand the observed BHSRs (see discussion in Croton et al. 2006; Saglia et al. 2016; Graham & Sahu 2023).

The Sloan Digital Sky Survey (SDSS) Mapping Nearby Galaxies at Apache Point Observatory (MaNGA, Bundy et al. 2015) project provides spatially resolved spectra of about 10,000 galaxies and offers an unprecedented opportunity to study star formation quenching and its relation to galaxy properties. The data can be used to obtain spatially resolved information about quenching and dynamical properties within individual galaxies, thus allowing more comprehensive analyses on the connection between quenching and structural and dynamical properties of galaxies. For example, recent studies based on MaNGA showed that quenching is inside-out, namely starts from the central region and spreads outwards (e.g. Li et al. 2015; Wang et al. 2018a; Ellison et al. 2018; Bluck et al. 2020b). Some galaxies are then expected to be quenched in central regions but star-forming in the outer parts. Investigating the connection between quenching and structural/dynamical properties in these hybrid galaxies is particularly valuable. Furthermore, we

can use the resolved spectroscopy to derive velocity dispersion in different parts of individual galaxies and use it as a parameter to establish a link to the observed BHSRs.

The paper is organized as follows. Section 2 briefly describes MaNGA, our sample selection and data reduction, in particular the method to define galaxies/objects of different quenching properties. In Section 3, we analyze the data and show that fully quenched galaxies and quenched central cores both follow the quenched galaxy scaling relation. We also investigate the dynamical status using the distribution of galaxies in space spanned by velocity dispersion measured in the inner and outer regions of galaxies. Section 4 presents discussions on an evolutionary track in dynamical status and quenching. We also discuss potential processes that can both change the dynamical status of galaxies and trigger AGN activities in them. In Section 5, we construct a toy model to connect quenching, the quenched galaxy scaling relation, BHSRs and AGN feedback. Finally, we summarize our results in Section 6. Throughout the paper, we adopt the following cosmological parameters:  $H_0 = 73\text{km/s/Mpc}$ ,  $\Omega_M = 0.3$  and  $\Omega_\Lambda = 0.7$ .

## 2. DATA AND ANALYSES

We describe galaxy samples used in our analyses in Section 2.1, and global and spatially resolved parameters of individual galaxies in Section 2.2. Section 2.3 shows how we classify galaxies based on their spatially resolved quenching properties. Section 2.4 describes a linear regression method used to analyze the observational data. Key symbols and terminologies used in this paper are listed in Table 1 for reference.

### 2.1. MaNGA galaxies and sample selection

Our galaxy sample is taken from Mapping Nearby Galaxies at Apache Point Observatory (MaNGA, Bundy et al. 2015) of Solan Digital Sky Survey Data Release 17 (SDSS DR17, Abdurro'uf et al. 2022). MaNGA galaxies are observed by the integral field units (IFUs) which have a wavelength coverage from 3600 Å to 10000 Å and a spectral resolution of about 2000. This enables us to analyze spatially resolved quenching and dynamical properties of galaxies. Over 10,000 galaxies have been observed during the period from April 2014 to August 2020, and the main MaNGA sample is selected to have a flat stellar mass distribution (Wake et al. 2017). The total data set consists of three sub-samples: Primary, Secondary and Color-Enhanced Samples, with Color-Enhanced Sample being a supplement of galaxies in the green valley. For Primary and Color-Enhanced Samples, the field of view (FOV) covers an aperture of  $1.5R_e$  or larger, where  $R_e$  is the effective (or half-light) radius of the galaxy, while the FOV of Secondary Sample covers an aperture of  $2.5R_e$  or larger. For the sake of comparison, our analyses are mainly based on galaxy properties within  $1.5R_e$ .

We adopt the data products of Pipe3D<sup>5</sup> (Sánchez et al. 2016a,b, 2022), which provides data for 10,220 galaxies from the analyses of 10,245 data cubes with 25 failed cases (some more information about the Pipe3D is given in the following subsection). MaNGA did some repeated

observations for spectrophotometric calibrations. For such cases, we choose data products with the highest signal-to-noise ratio (S/N) in the stellar mass ( $M_*$ ) measurement. We remove galaxies that do not have valid NSA redshifts or  $R_e$ , which results in a total of 9,988 galaxies. We also apply two further restrictions: (i) excluding galaxies with QCFLAG equal to 1 or 2, i.e. galaxies with wrong redshift or low S/N, or with no value listed for QCFLAG from spectral fitting; (ii) galaxies are required to have valid measurements for the central velocity dispersion ( $\sigma_{\text{in}}$ ), velocity dispersion in the outskirts ( $\sigma_{\text{out}}$ ) and the star formation rate (SFR). With these two restrictions, a total of 9,591 galaxies remain.

To have a galaxy sample that may be less affected by environmental processes, we focus on central galaxies in galaxy groups and clusters. To achieve this, we cross-match the Pipe3D catalog with the SDSS group catalog provided by Yang et al. (2007). We obtain 8,888 galaxies, among which 6,231 are centrals. We only consider galaxies with  $\log M_*/M_\odot \geq 10$ , because star formation quenching plays a less important role in these low-mass centrals. Our final central galaxy sample consists of 5,124 galaxies, with stellar mass covering the range  $10^{10.0} - 10^{12.2}M_\odot$ .

Our analyses also use optically-selected AGNs, radio galaxies and barred galaxies. To obtain an optical AGN subsample, we first cross-match our sample galaxies with the MPA-JHU catalog (Brinchmann et al. 2004; Kauffmann et al. 2003) to obtain the fluxes in four emission lines: H $\alpha$ , H $\beta$ , [NII] $\lambda$ 6584 and [OIII] $\lambda$ 5007. We then use the the BPT diagnostic diagram to identify 578 galaxies that are classified as optical AGNs according to the criterion proposed by Kewley et al. (2001). We cross-match our galaxies with the radio source catalog provided by Best & Heckman (2012) and obtain 156 radio galaxies. To select barred galaxies, we cross-match our sample galaxies with the Galaxy Zoo DR2 (GZ2) catalog (Willet et al. 2013; Hart et al. 2016), and identify barred galaxies as the ones with `t03_bar_a06_bar_flag=1`, as recommended by GZ2. This yields a subsample of 421 barred galaxies. In the following, we also investigate the  $r$ -band Sérsic index,  $n$ , taken from the NYU value-added galaxy catalog (NYU-VAGC, Blanton et al. 2005).

### 2.2. Measurements from Pipe3D

Pipe3D provides a comprehensive analysis of both stellar continuum and gas emission lines. For our study, we use the newly released data products derived from pyPipe3D (Sánchez et al. 2022). Pipe3D analyzes the data cubes sampled linearly in wavelength and pre-processes them with Galactic extinction and a normalised spectral resolution. Due to a minimum S/N requirement for the analysis, contiguous spaxels are grouped together to make a spatial bin (tessella). Pipe3D first performs a simple stellar population (SSP) fitting to the stellar continuum. The SSP spectrum is shifted according to the mean stellar velocity, multiplied by the Cardelli extinction curve (Cardelli et al. 1989) to account for dust extinction, and convolved with a Gaussian function to account for stellar velocity dispersion ( $\sigma$ ). The MaStar\_sLOG library (Yan et al. 2019) sampled by 273 SSP spectra with 39 ages (from 1 Myr to 13.5 Gyr) and 7 metallicities (from 0.006  $Z_\odot$  to 2.353  $Z_\odot$ ), and the Salpeter (Salpeter 1955) initial mass func-

<sup>5</sup> <https://data.sdss.org/sas/dr17/manga/spectro/pipe3d/v3.1-1/3.1.1/>

TABLE 1  
TERMINOLOGIES AND SYMBOLS

Terminology	Criterion and description
FQG	$f_q > 95\%$ , fully quenched galaxy
PQG	$5\% \leq f_q \leq 95\%$ , partially quenched galaxy
FSG	$f_q < 5\%$ , fully star-forming galaxy
QCC	$\bar{f}_q = 95\%$ , $R_q > 4''$ , quenched central core
SRDH	scaling relation of dynamical hotness
QGSR	quenched galaxy $M_*$ - $\sigma_{\text{in}}$ scaling relation
BHSR	supermassive black hole scaling relation
Symbols	Description
$M_*$	stellar mass of a galaxy in FOV
$R_e$	$r$ -band half-light radius of a galaxy or QCC
$n$	$r$ -band Sérsic index of a galaxy
sSFR	$\text{H}\alpha$ -based specific star formation rate in FOV
$M_q$	stellar mass of a QCC
$R_q$	size of a QCC
$\bar{f}_q$	quenched fraction in $1.5R_e$ or in $R_q$
$\sigma(R)$	velocity dispersion profile
$\sigma_{\text{in}}$	median $\sigma$ of spaxels within $0.2R_e$
$\sigma_{\text{out}}$	median $\sigma$ of spaxels in $1.4R_e < R < 1.5R_e$
$\Sigma_1$	surface mass density in central 1 kpc
$\sigma_{\text{hot}}$	$\log \sigma_{\text{hot}} = 0.3 \log M_* - 1.1$ (SRDH, Eq. 4)
$\sigma_q$	$\log \sigma_q = 0.30 \log M_* - 1.02$ (QGSR, Eq. 5)
$\alpha$	$\alpha = 0.30$ , the slope of the QGSR
$\beta$	$\beta = -1.02$ , the intercept of the QGSR
$\Delta_q$	$\Delta_q = 0.08$ , the intrinsic scatter of the QGSR

tion (IMF), are adopted by Pipe3D. The modelled stellar spectrum is then subtracted from the observed one to obtain a ‘pure-GAS spectrum’ that consists of emission lines, noise and residuals from the first (SSP-fitting) step. Strong emission lines in each spaxel are fitted with individual Gaussian functions. Pipe3D runs a series of Monte Carlo iterations with the input spectrum perturbed with its errors. The parameters quoted later are the mean values of the results from the iterations, and the corresponding errors are the standard deviations that account for both the noise and uncertainties in the fitting.

Spatially resolved parameters are the direct products of Pipe3D. The stellar velocity dispersion ( $\sigma$ ) for each spaxel is obtained simultaneously in the SSP fitting. The mass-to-light ratio and surface brightness can be used to estimate the surface mass density ( $\Sigma_*$ ) of each spaxel. The 4000Å break (D4000) is defined as the flux ratio between the red and blue sides of  $\lambda 4000\text{\AA}$ , as in Bruzual A. (1983) and Gorgas et al. (1999). This definition is less sensitive to smearing by velocity dispersion than the narrow version (Sánchez et al. 2016b; Bluck et al. 2020a). The amplitude of D4000 is believed to be a good indicator of stellar age (see e.g. Kauffmann et al. 2003), and we use it to define quenching properties for each spaxel (see Section 2.3). Pipe3D provides two sets of mask extensions: the first is the GAIA\_MASK extension, which masks spaxels that are impacted by bright field stars; the second is the SELECT\_REG extension, which masks spaxels with low S/N spectra.

Pipe3D also provides global parameters for each galaxy. Some of them are directly taken from the NSA catalog, such as redshift, effective radius ( $R_e$ ), position angle (PA) and ellipticity (Blanton et al. 2011). In Pipe3D, ellipticity is defined as  $\sqrt{1 - (b/a)^2}$ , where  $b$  and  $a$  are the lengths of minor and major axes, respectively. The effective radius,  $R_e$ , is defined as the Petrosian half-

light radius in the  $r$ -band, and PA is defined as direction in which the major axis lies. The ellipticity is an indicator of the inclination of a disk galaxy and the shape of an elliptical galaxy. We use these parameters to estimate their profiles and other properties of individual galaxies. The integrated quantities, such as stellar mass ( $M_*$ ) and star formation rate (SFR), are also provided by Pipe3D by adding corresponding values of individual spaxels within the whole field of view (FOV) of the corresponding IFU, excluding masked spaxels. The dust-corrected  $\text{H}\alpha$  luminosity of a spaxel is used to estimate the star formation rate surface density ( $\Sigma_{\text{SFR}}$ ) using the relation given by Kennicutt (1998). Pipe3D coadds the  $\Sigma_{\text{SFR}}$  within the FOV to derive the integrated star formation rate ( $\text{SFR}_{\text{H}\alpha}$ ). Note that Pipe3D does not exclude  $\text{H}\alpha$  emission that is not from young massive stars. The  $\text{SFR}_{\text{H}\alpha}$  may thus represent an upper limit for some galaxies. Pipe3D also provided  $\text{SFR}_{\text{SSP}}$  using three different timescales (10, 32 and 100 Myr) based on the SSP analysis. Tests show that these SFRs are strongly correlated, although there are some systematic offsets. In this paper, we adopt the SFR estimated from the  $\text{H}\alpha$  emission line. The specific star formation rate (sSFR) is defined as  $\text{SFR}/M_*$ . All the parameters are listed in Table 1 along with their definitions.

For values adopted directly from Pipe3D, we use the corresponding measurement errors provided by Pipe3D to represent the statistical uncertainties in our analyses. Pipe3D does not provide measurement errors for  $R_e$ , and we follow Sahu et al. (2020) to assume a 30% uncertainty for this quantity. This uncertainty for  $R_e$  is used in modeling the  $M_*$ - $R_e$  relation in Section 3.3, and our tests show that the result is not sensitive to the choice of the uncertainty.

To derive parameters from the spatially resolved products of Pipe3D, it is necessary to check the quality of the data for this purpose. Among all spaxels within  $1.5R_e$  of our selected galaxies, about 0.14% and 3.99% are in GAIA\_MASK and SELECT\_REG masks, respectively. Our tests show that Pipe3D products for most of the unmasked spaxels have relatively good qualities. Among all the 5,124 galaxies, 4,978 of them have all their spaxels in  $1.5R_e$  with  $S/N > 5$  in D4000; 4,387 galaxies have all spaxels with  $S/N > 3$  in  $\Sigma_*$ ; and 3,509 galaxies have all spaxels with  $S/N > 3$  in  $\sigma$ . This indicates that  $\sigma$  is more sensitive to spectral qualities than the other two quantities. Our further test shows that, in 80% of the sample galaxies, more than 85% of their spaxels have  $S/N > 3$  in  $\sigma$ . In our analyses, we exclude spaxels with  $S/N \leq 3$  in  $\sigma$ .

We derive the profile of a parameter using selected spaxels within the central  $1.5R_e$ , and the observed PA and ellipticity are used to make the inclination correction (see e.g. Bluck et al. 2020b). For example, for each galaxy, we use the median value of  $\sigma$  in an inclination-corrected annulus to calculate the  $\sigma$  profile. The related global parameter of the galaxy is obtained from the profile. For instance, the central velocity dispersion ( $\sigma_{\text{in}}$ ) is defined as the median value of  $\sigma$  within the central  $0.2R_e$  and the velocity dispersion in the outskirts ( $\sigma_{\text{out}}$ ) is the median  $\sigma$  within  $1.4$ - $1.5R_e$ . The central stellar mass surface density ( $\Sigma_1$ ) is calculated by first coadding the  $\Sigma_*$  of spaxels within the central 1 kpc (also inclination corrected) and then dividing it by the summation

of the physical areas of the spaxels. The profiles of the quenched fraction shown in the next section are also calculated using inclination-corrected annuli. We list these parameters and their descriptions in Table 1 for reference.

For a quantity,  $S$ , derived from the measurements of a set of individual spaxels, we use the following procedure to obtain its uncertainty. For each spaxel in the set, the measurement of the relevant spaxel quantity,  $s$ , and the corresponding uncertainty,  $e_s$ , both given by Pipe3D, are used to generate a new  $s'$  from  $N(s, e_s^2)$  using a Monte Carlo method. The set of the Monte-Carlo generated  $s'$  values are then used to derive an  $S'$  in the same way as  $S$  is obtained. We repeat this process 500 times to obtain the distribution of  $S'$  and use the standard deviation of the distribution to represent the uncertainty of the derived quantity. For example,  $\sigma_{\text{in}}$  and  $\sigma_{\text{out}}$  are defined as the median values of the  $\sigma$  in the corresponding sets of spaxels, so that their errors are obtained from the variances of the medians of the 500 Monte Carlo samples. We note again that this procedure is valid only under the assumption that the uncertainties in different spaxels are independent.

### 2.3. Classification of galaxies

As shown in the left panel of Figure 1, the D4000 distribution of spaxels is bimodal, with a valley around 1.55. Since the D4000 of a spaxel is strongly correlated with its SFR surface density (e.g. Brinchmann et al. 2004), we use  $D4000_{\text{th}} = 1.55$  to separate spaxels into two categories, quenched and star-forming. We define the quenched fraction,  $f_q$ , as the fraction of spaxels with  $D4000 > D4000_{\text{th}}$ . For each galaxy, we calculate the mean quenched fraction,  $\bar{f}_q$ , within  $1.5R_e$ , as well the quenched profile,  $f_q(R)$ , which is the quenched fraction as a function of the radius to the galaxy center. The  $\bar{f}_q$  distribution of galaxies, plotted in the right panel of Figure 1, peaks towards the two extremes, suggesting that quenching usually occurs over the entire galaxy (see also, Wang et al. 2018a; Bluck et al. 2020a). Based on this distribution, we classify galaxies into several classes in a way similar to that proposed in Wang et al. (2018a). Fully quenched galaxies (FQGs) are defined as the ones with  $\bar{f}_q > \bar{f}_{q,\text{th}} = 0.95$ . In this class, the majority of the spaxels within  $1.5R_e$  are quenched spaxels. Fully star-forming galaxies (FSGs) are defined as the ones that have  $\bar{f}_q < 1 - \bar{f}_{q,\text{th}} = 0.05$ , i.e. the majority of their spaxels are classified as star-forming spaxels. The rest of the galaxies are classified as partially quenched galaxies (PQGs). This classification results in 1,672 FQGs, 1,879 FSGs, and 1,573 PQGs. The acronyms are listed in Table 1 for reference.

The median quenched profiles for galaxies in different bins of  $\bar{f}_q$  are shown in Figure 2. We can see that  $\bar{f}_q$  is about one at small radii for all cases, and drops at larger radii. The drop is quite rapid for galaxies with low  $\bar{f}_q$ . This suggests that a PQG usually has a fully quenched core in its center. We can thus define a minimum radius, within which the quenched fraction is equal to  $\bar{f}_{q,\text{th}}$ . We refer to this radius as the quenched radius, denoting it as  $R_q$ . The mass  $M_q$  of the quenched central core (QCC) is defined as the sum of the stellar mass within  $R_q$ . We assume that the fractional errors in  $M_q$  and  $R_q$  are the

same as  $M_*$  and  $R_e$ , respectively. In the calculation, a spaxel without  $\Sigma_*$  measurement is given the median value of the spaxels that have the same radius as the spaxel. We only consider QCCs with  $R_q \geq 4''$  to ensure that the cores can be well resolved and our measurements are not significantly contaminated by structures larger than  $R_q$ . We also try to identify QCCs in FSGs with non-zero  $\bar{f}_q$ , but they are too small to meet the criterion of  $R_q \geq 4''$ . Thus, QCCs are identified only in PQGs. For each QCC, we define its  $\sigma_{\text{in}}$  as the median  $\sigma$  of the spaxels within  $0.2R_e$  and  $\sigma_{\text{out}}$  as the median  $\sigma$  in  $1.4-1.5R_e$ , where  $R_e$  for QCCs are defined in Section 3.3. Sixty one QCCs do not have valid  $\sigma_{\text{in}}$  or  $\sigma_{\text{out}}$  measurements and are excluded. This leaves a total of 599 QCCs for our analyses.

We have performed a series of tests with various  $D4000_{\text{th}}$  and  $\bar{f}_{q,\text{th}}$  to check whether our results are sensitive to the choices of these thresholds. These tests are based on nine combinations of three choices of  $D4000_{\text{th}}$  (1.5, 1.55 and 1.6) and three choices of  $\bar{f}_{q,\text{th}}$  (0.9, 0.95 and 0.98). Most of the results shown in this paper are affected only slightly, and our conclusions remain unchanged. As shown in Figure 1, D4000 has a bimodal distribution, and a small variation of  $D4000_{\text{th}}$  around the valley ( $\sim 1.55$ ) does not lead to a significant change in the sample classification. The distribution of  $\bar{f}_q$ , shown in the right panel of Figure 1 using  $D4000_{\text{th}} = 1.55$ , is also strongly bimodal, and so a small change in  $\bar{f}_{q,\text{th}}$  does not lead to any significant changes in our conclusions.

### 2.4. Correlation analyses

Our investigation also uses correlations between galaxy properties described above, and here we describe the related analyses. Suppose that we have two series of data points,  $X = \{x_1, \dots, x_n\}$  and  $Y = \{y_1, \dots, y_n\}$ , with the elements,  $x_i$  and  $y_i$ , representing two properties of galaxy  $i$  in the sample of  $n$  galaxies. The uncertainties of the measurements are represented by the standard deviations,  $e_{xx,i}$  and  $e_{yy,i}$ . In many cases, we assume a linear relation between  $Y$  and  $X$ , and we write

$$Y = a_1X + a_2 + N(0, \Delta^2), \quad (1)$$

where  $a_1$  is the slope,  $a_2$  is the intercept, and we model the variance in the relation by  $N(0, \Delta^2)$ , a normal distribution with mean equal to 0 and variance equal to  $\Delta^2$ . Thus,  $\Delta$  describes the intrinsic scatter of the relation in  $Y$ . To constrain the three free parameters,  $a_1$ ,  $a_2$  and  $\Delta$ , we construct a posterior distribution as,

$$\text{Posterior} = \text{Likelihood} \times \text{Prior}. \quad (2)$$

Taking into account of measurement uncertainties and intrinsic scatter, we write the likelihood term as,

$$\text{Likelihood} = \prod_{i=1}^n \frac{1}{\sqrt{2\pi(e_{yy,i}^2 + a_1^2 e_{xx,i}^2 + \Delta^2)}} \times \exp\left\{-\frac{[y_i - (a_1x_i + a_2)]^2}{2(e_{yy,i}^2 + a_1^2 e_{xx,i}^2 + \Delta^2)}\right\}. \quad (3)$$

Given that we have little prior information about the free parameters, we take uninformative *priors*, i.e. a flat distribution in a given range. We use the python code `emcee` (Goodman & Weare 2010; Foreman-Mackey et al.

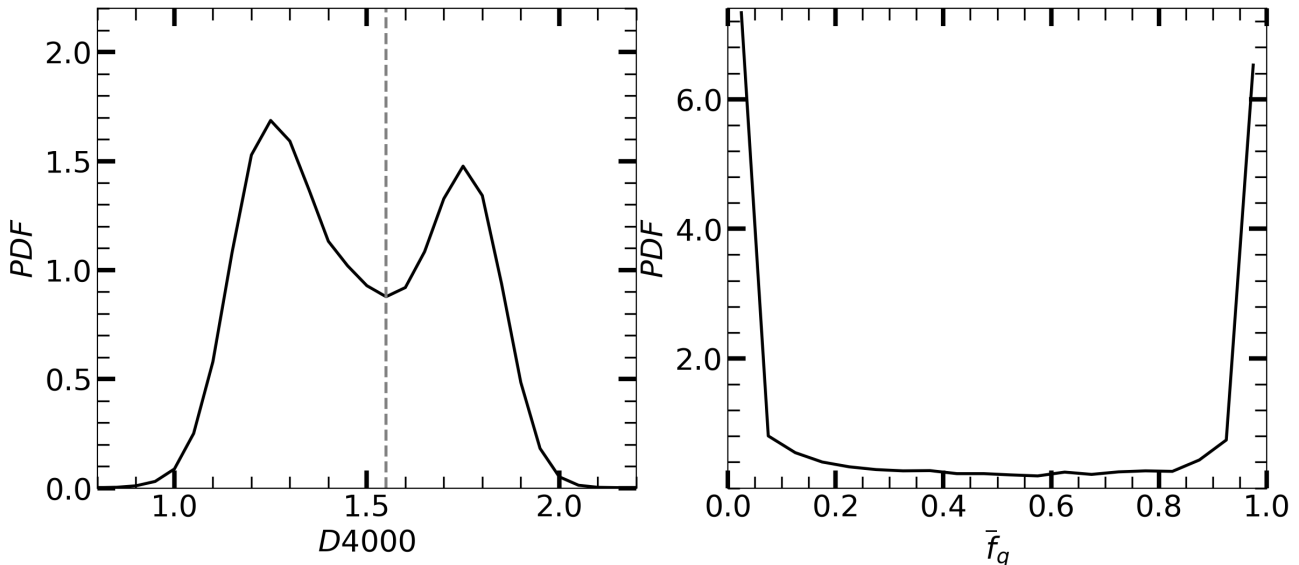


FIG. 1.— Probability distribution functions of spatially resolved D4000 (left panel) and mean quenched fraction ( $\bar{f}_q$ , right panel) for our galaxy sample. In the left panel, we show the result for D4000 of spaxels within  $1.5R_e$  and the grey dashed line indicating  $D4000_{\text{th}} = 1.55$ . In the right panel,  $\bar{f}_q$  is calculated with  $D4000_{\text{th}} = 1.55$ .

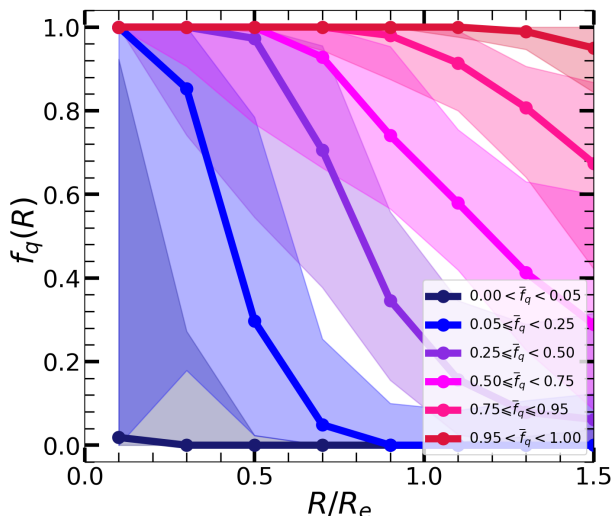


FIG. 2.— The median quenched profiles ( $f_q(R/R_e)$ ) for galaxies with different  $\bar{f}_q$  bins as indicated in the figure. The shadows show the 16th and 84th percentiles of the distribution of  $f_q$ . Note that galaxies with  $\bar{f}_q < 0.05$  are FSGs (dark blue), galaxies with  $\bar{f}_q > 0.95$  are FQGs (red), the rest galaxies are PQGs. We do not show galaxies with  $\bar{f}_q = 0$  or  $\bar{f}_q = 1$ .

2013), which is the implementation of the ensemble sampler for Markov Chain Monte Carlo (MCMC), to sample the distribution of the model parameters.

### 3. DYNAMICAL HOTNESS AND STAR FORMATION QUENCHING

#### 3.1. Defining dynamical hotness

As discussed above, the quenching status of a galaxy is correlated with its dynamical state. Here we define the dynamical hotness of a galaxy to characterize the randomness of stellar motion. Historically, galaxies obeying the Faber-Jackson relation (FJR) are called hot dynamical systems (see e.g. Bender et al. 1992), and we adopt a similar relation to define dynamical hotness. Figure

3 shows  $\sigma_{\text{in}}$  versus  $M_*$  for all our sample galaxies. For comparison, we also show the FJR obtained by Gallazzi et al. (2006) and Oh et al. (2020). The slopes of the two FJR are very similar, 0.286 and 0.285, respectively, and the zero points differ by less than 0.05 dex in  $\sigma_{\text{in}}$ . One can see, both FJR describe well the trend followed by the hottest population with the highest  $\sigma_{\text{in}}$  at given  $M_*$  in our MaNGA sample. However, the two FJR were obtained using  $M_*$  and  $\sigma_{\text{in}}$  measured in different ways from ours. It is thus necessary to re-calibrate the relation for our purpose.

Pipe3D provides morphology classification using a machine learning method based on several galaxy features, including Sérsic index, stellar mass, line-of-sight  $V - \sigma$  ratio,  $R_e$ , ellipticity, concentration and  $ugriz$  colors (Sánchez et al. 2022). We select galaxies identified as ellipticals to represent dynamically hot galaxies. However, our visual inspection shows that some of the elliptical galaxies listed as Pipe3D are actually face-on spirals and have very small  $\sigma_{\text{in}}$ . This mis-classification is severer for lower-mass galaxies, and the classification is more reliable at the massive end. We thus decide to use massive galaxies for our calibration. There are 158 galaxies with  $\log M_*/M_\odot > 11.5$  classified as ellipticals. We remove galaxies with close companions and/or significant asymmetrical structure. The remaining 103 ellipticals are shown in Figure 3 as the pink points. We then use a linear relation with a slope of 0.3 to fit these elliptical galaxies. We fix the slope because previous studies usually gave similar slopes (see e.g. Gallazzi et al. 2006; Oh et al. 2020). The scaling relation obtained is

$$\log \sigma_{\text{hot}} = 0.3 \log M_* - 1.1 \quad (4)$$

(see also Table 1). This relation is shown in Figure 3 as the pink line. For clarity, we will refer to Equation 4 as the scaling relation of dynamical hotness (or SRDH). As one can see, our SRDH is very close to the FJR obtained previously. We have also performed the same fitting to the total 158 elliptical galaxies and obtained a

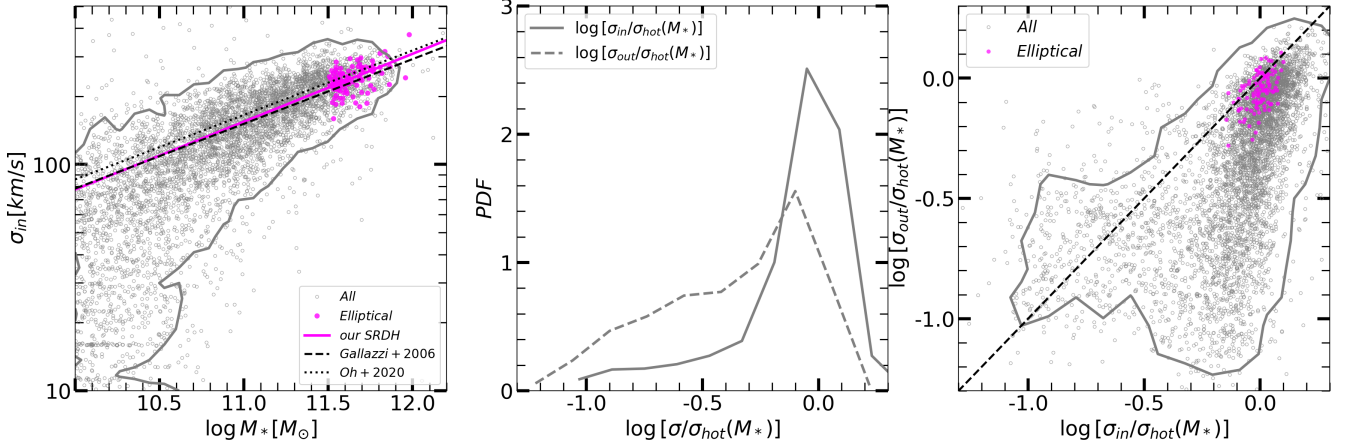


FIG. 3.— Left panel:  $\sigma_{in}$  versus  $M_*$ . The pink solid line represents the SRDH (Equation 4). Its slope is fixed to 0.3 and its amplitude is determined by massive ( $M_* > 10^{11.5} M_\odot$ ) elliptical galaxies (pink solid circles). Grey circles show all galaxies used in this paper and grey line corresponds to the 95%-th contour level. The black dashed (Gallazzi et al. 2006), dotted (Oh et al. 2020) lines are the Faber-Jackson relation taken from literature for comparison. Middle panel: Probability distribution functions of  $\log(\sigma_{in}/\sigma_{hot})$  (grey solid line) and  $\log(\sigma_{out}/\sigma_{hot})$  (grey dashed line) for all galaxies. Right panel: the Two- $\sigma$  diagram,  $\sigma_{in}/\sigma_{hot}$  versus  $\sigma_{out}/\sigma_{hot}$ . Symbols are the same as that in the left panel except that the black dashed line shows the 1:1 relation.

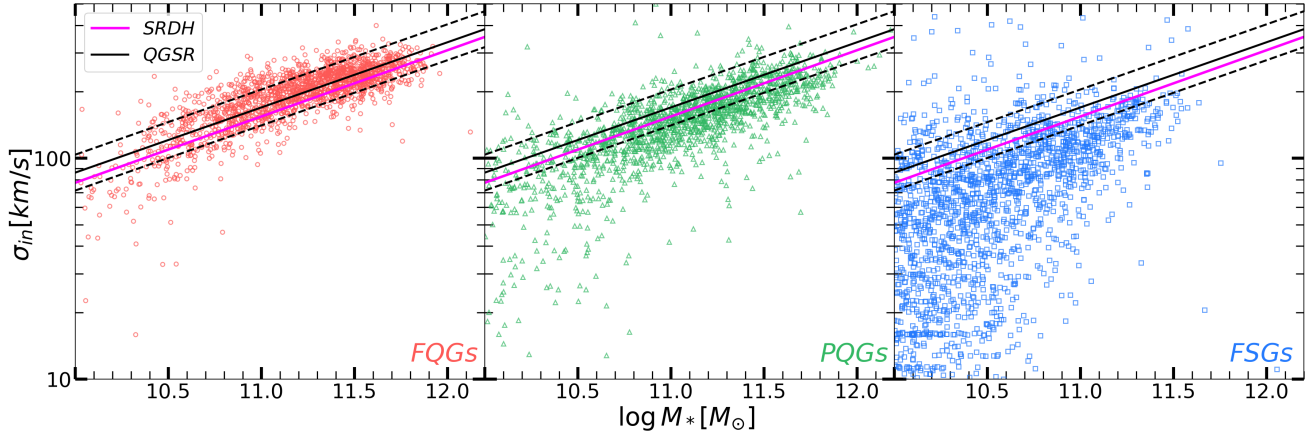


FIG. 4.— Central velocity dispersion ( $\sigma_{in}$ ) versus stellar mass ( $M_*$ ) for three different classes of galaxies, FQGs (left: red circles), PQGs (middle: green triangles) and FSGs (right: blue squares). The pink solid line is the SRDH (Equation 4). The black solid line shows the best fitting for FQGs (Equation 5), i.e. quenched galaxy scaling relation (QGSR). The black dashed lines represent the  $1-\Delta$  intrinsic scatter of this relation.

very similar result. As one can also see, the SRDH basically defines an upper boundary of the velocity dispersion at a given stellar mass, as expected from a dynamically hot system in which the structure is supported predominantly by the random motion of stars.

In what follows, we use the deviation of a galaxy from the SRDH to define the dynamical hotness of a galaxy. Specifically, we use the ratio of the measured velocity dispersion of a galaxy to the value of  $\sigma_{hot}$  obtained from its stellar mass to characterize its hotness. The middle panel of Figure 3 shows the probability distributions of  $\sigma_{in}/\sigma_{hot}$  and  $\sigma_{out}/\sigma_{hot}$ . We can see that  $\log(\sigma_{in}/\sigma_{hot})$  peaks around zero, with an extended tail down to  $-1$ . Compared to  $\sigma_{in}/\sigma_{hot}$ ,  $\sigma_{out}/\sigma_{hot}$  shows a much more extended distribution and a much lower peak, indicating that the dynamical hotness may depend on the distance to the center in an individual galaxy. Clearly, the dynamical hotness in outer part of a galaxy provides additional information about the dynamical status of the galaxy. In the right panel of Figure 3 we show  $\sigma_{in}/\sigma_{hot}$  versus  $\sigma_{out}/\sigma_{hot}$  (hereafter, the Two- $\sigma$  diagram). As one

can see, galaxy distribution in this diagram appears to be concentrated in two branches: a nearly horizontal branch in which  $\sigma_{out}/\sigma_{hot}$  is low, and a nearly vertical branch in which  $\sigma_{in}/\sigma_{hot}$  is close to one. Elliptical galaxies used to calibrate the SRDH are located in a small region around  $\log(\sigma_{in}/\sigma_{hot}) \sim 0$  and  $\log(\sigma_{out}/\sigma_{hot}) \sim 0$ , so that they are dynamically hot over their entire bodies. As we will see in Section 3.4, galaxies of different quenching status show distinctive distributions in the Two- $\sigma$  diagram, making the diagram a powerful tool to understand quenching processes (see also Section 4).

### 3.2. Dynamical hotness and quenching status

Figure 4 shows the central velocity dispersion versus the stellar mass for fully quenched galaxies (FQGs, left panel), partially quenched galaxies (PQGs, middle panel), and fully star-forming galaxies (FSGs, right panel). As one can see, FQGs exhibit a strong and tight correlation between  $\sigma_{in}$  and  $M_*$ . Using the same method described in Section 2.4, we fit the relation to a power-

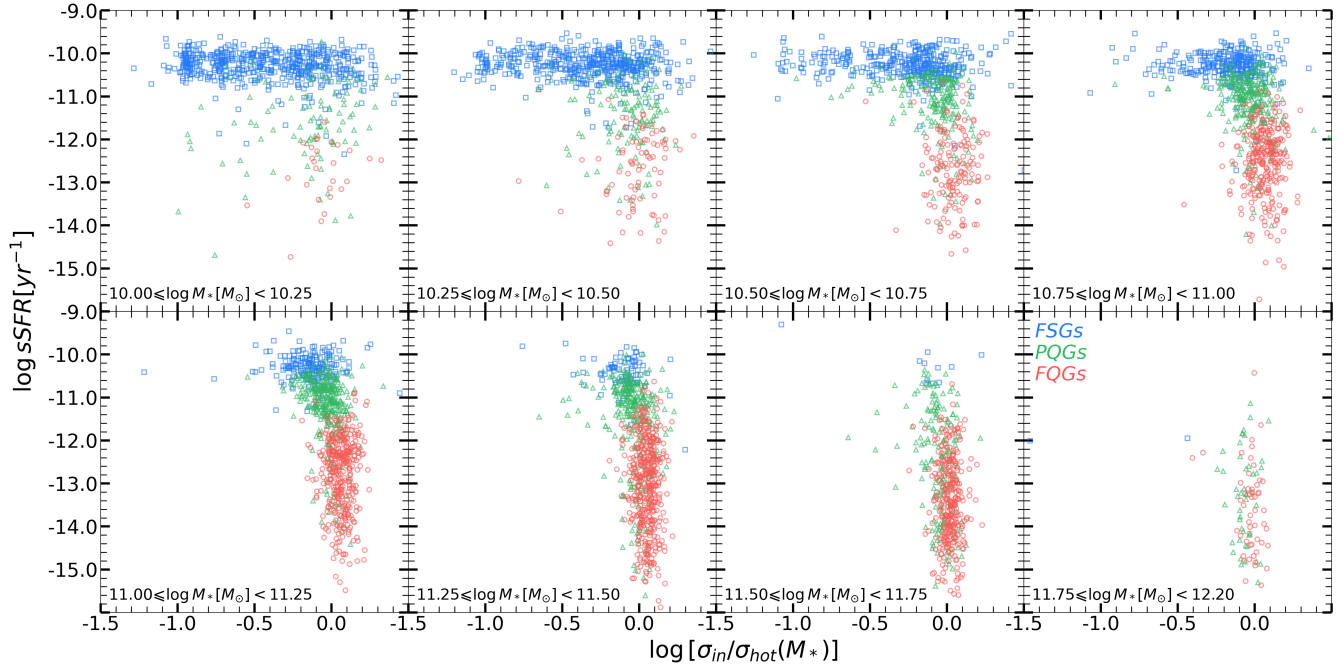


FIG. 5.— The sSFR as a function of  $\log(\sigma_{\text{in}}/\sigma_{\text{hot}})$  for FQGs (red circles), PQGs (green triangles) and FSGs (blue squares). Galaxies of different stellar masses are shown in different panels.

law function (Equation 1) and obtain

$$\log \sigma_{\text{q}} = \alpha \log M_{*} + (\beta \pm \Delta_{\text{q}}), \quad (5)$$

with  $\alpha = 0.30$ ,  $\beta = -1.02$ , and  $\Delta_{\text{q}} = 0.08$  (Table 1). This scaling relation is referred to as the quenched galaxy scaling relation (QGS). The QGS is similar to the relation for red galaxies obtained by Fang et al. (2013). It is also very similar to the SRDH defined above to represent dynamically hot galaxies (Figure 4). This clearly shows that the FQGs are all dynamically hot in their central regions (see also Section 3.4).

The  $M_{*} - \sigma_{\text{in}}$  relation for FSGs is very different from that for FQGs: at given  $M_{*}$  the  $\sigma_{\text{in}}$  distribution is much broader. The majority of FSGs have lower  $\sigma_{\text{in}}$  than FQGs, in particular at small  $M_{*}$ . This is expected, as a large fraction of FSGs are spiral galaxies that have small bulges and low velocity dispersion in inner regions. A small fraction of FSGs are close to the SRDH, and some even have  $\sigma_{\text{in}}$  above the SRDH. As we will discuss in Section 4, the existence of these centrally hot star-forming galaxies has important implications for galaxy quenching and the related processes. The PQGs follow a  $M_{*} - \sigma_{\text{in}}$  relation that lies in between the FQG and FSG populations. For a given  $M_{*}$ , their  $\sigma_{\text{in}}$  is, on average, only slightly lower than the SRDH. A significant fraction of PQGs lie above the SRDH, indicating that they are dynamically hot in their inner regions. The different  $\sigma_{\text{in}}$  distributions among the three populations indicate that quenching processes may be related to the velocity dispersion of the central stellar components, as suggested in some previous studies (e.g. Fang et al. 2013; Bluck et al. 2020a; Brownson et al. 2022).

To see the relation between star formation and dynamical hotness more clearly, we show the specific star formation rate as a function of  $\sigma_{\text{in}}/\sigma_{\text{hot}}$  for six narrow  $M_{*}$  bins in Figure 5. As one can see, most of the FQGs have low star formation activities, with  $\log \text{sSFR} < -12$ , and are

dynamically hot in the inner region, with  $\sigma_{\text{in}}/\sigma_{\text{hot}} \sim 1$ . Note that the sSFR distribution of FQGs is very broad, ranging from  $\log \text{sSFR} = -12$  to  $-15$ , indicating that some of these galaxies may still have some low-level star formation activity that is not correlated with  $\sigma_{\text{in}}$ .

In contrast, FSGs have a very narrow distribution in sSFR, with  $-9.5 > \log \text{sSFR} > -10.6$ , almost independent of stellar mass, indicating that they follow well the star-forming main sequence. The  $\sigma_{\text{in}}$ -distribution of these galaxies is very broad, ranging from less than  $0.1\sigma_{\text{hot}}$  to  $\sim \sigma_{\text{hot}}$ , and the width of the distribution decreases with increasing stellar mass. Thus, FSGs of higher  $M_{*}$ , on average, follow the SRDH more closely. This is consistent with the fact that central components of spiral galaxies become more concentrated and bulge-dominated as  $M_{*}$  increases (see e.g. Barro et al. 2017). There is no significant correlation between  $\sigma_{\text{in}}$  and sSFR for FSGs. Overall, FSGs appear to form a horizontal sequence (in the  $\sigma_{\text{in}}/\sigma_{\text{hot}}$ -sSFR plane) that is almost perpendicular to the almost vertical sequence defined by the FQG population.

There is a clear gap between the two sequences defined by FQGs and FSGs, which is bridged by PQGs, as shown by the green points in in Figure 5. The sSFR distribution of the PQG population is actually very broad, touching the sequence defined by FSGs and having a long tail extended well into the sequence defined by FQGs. PQGs with  $\log \text{sSFR} < -12$  have almost the same  $\sigma_{\text{in}}$  distribution as FQGs and their sSFR is also quite independent of  $\sigma_{\text{in}}$ . These PQGs usually have large  $f_{\text{q}}$ , and overlap with the FQG population in many properties, as we will show later. These results suggest that PQGs with low sSFR are either on their way to become FQGs in the near future or are FQGs that have acquired some star-forming gas in the recent past. This sub-population consists of 375 galaxies, less than a quarter of the total PQG population. For the rest 3/4 of the PQG population with



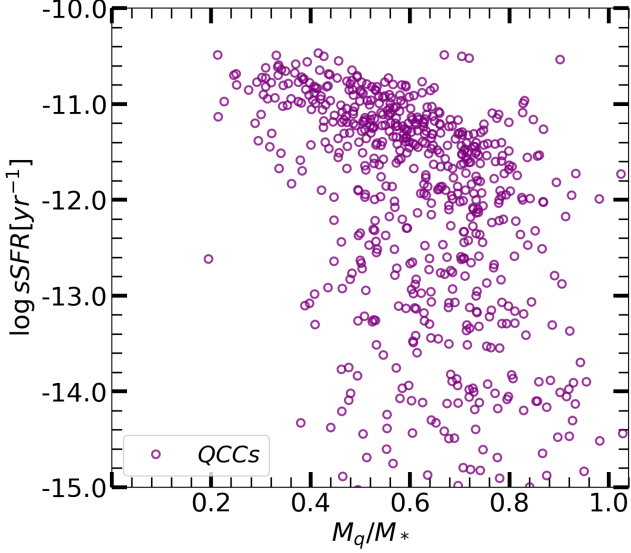


FIG. 6.— The sSFR versus  $M_q/M_*$  for QCCs. The sSFR is measured within the whole galaxy rather than within the QCC.

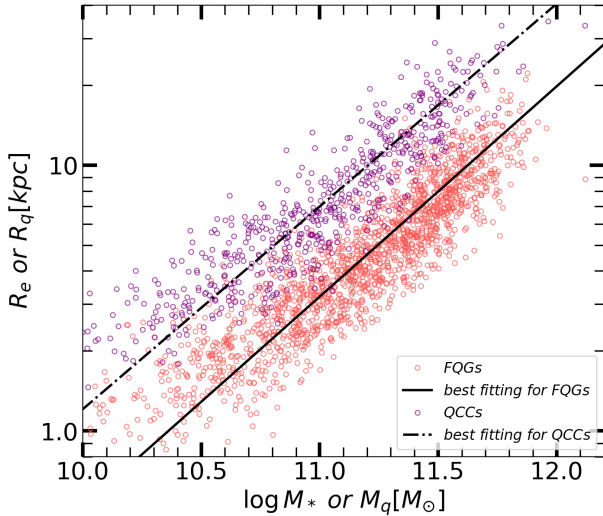


FIG. 7.— Red circles:  $R_e$  versus  $M_*$  for FQGs. Purple circles:  $R_q$  versus  $M_q$  for QCCs. The solid and dash-dotted lines show the best-fitting results for FQGs and QCCs respectively.

$\log \text{sSFR} > -12$ , there is a noticeable negative trend of sSFR with  $\sigma_{\text{in}}/\sigma_{\text{hot}}$  for  $\log(M_*/M_\odot) > 10.5$ . As shown in Section 3.3, many of these galaxies possess a quenched central core (QCC; see also Figure 2), and the mass of the QCC increases with  $\sigma_{\text{in}}$ .

The three populations together form an L-shaped pattern in the sSFR- $\sigma_{\text{in}}$  plane. This L-shape is well-defined in all stellar mass bins, except a tiny fraction of low mass galaxies residing at the lower-left corner (we will discuss these galaxies in Section 4.3). This is consistent with the results of Fang et al. (2013) and Barro et al. (2017) based on stellar mass surface densities. The L-shape suggests a transition in the evolution of star formation and its relation to dynamical hotness. It shows that a galaxy is fully quenched only when it has evolved to a dynamical state that is close to the SRDH. It is widely believed that  $\sigma_{\text{in}}$  is strongly correlated with the mass of the supermassive black hole (SMBH) residing in galaxy center

(Kormendy & Ho 2013). Our results may thus suggest that a galaxy can be fully quenched only after its SMBH mass has reached to a certain level that has been found in simulations (Zinger et al. 2020; Terrazas et al. 2020; Piotrowska et al. 2022). We will come back to this in Section 5.

### 3.3. Quenched central cores

Recent IFU observations suggest that in many galaxies quenching of star formation is inside-out (e.g. Li et al. 2015; Wang et al. 2018a). This can also be seen in Figure 2, which shows that PQGs usually have fully quenched cores in their centers while remain star-forming in outer parts. The ratio between the QCC mass,  $M_q$ , and  $M_*$  increases with  $\bar{f}_q$ , with the median  $M_q/M_* \approx 0.46$ , 0.56 and 0.70 for  $0.05 \leq \bar{f}_q < 0.33$ ,  $0.33 \leq \bar{f}_q < 0.66$ ,  $0.66 \leq \bar{f}_q \leq 0.95$ , respectively. Figure 6 shows the sSFR as a function of  $M_q/M_*$ . At  $\log \text{sSFR} > -12$ , the relation shows a clear negative trend that the sSFR of a galaxy decreases as the mass fraction of the QCC increases. At  $\log \text{sSFR} < -12$ , no significant correlation can be seen between sSFR and  $M_q/M_*$ . As discussed above and shown in Figure 5, PQGs with  $\log \text{sSFR} < -12$  have properties similar to those of FQGs.

We calculate the central velocity dispersion for QCCs using the same method as for galaxies. To do this, we need to know the radius,  $R_e$ , for each QCC, which can be calculated from  $R_q$  as defined in Section 2.3. Figure 7 shows  $R_q$  versus  $M_q$ . For comparison, we also include the  $R_e$ - $M_*$  relation for FQGs. Both FQGs and QCCs follow a tight mass-size relation. At the same mass,  $R_q$  of QCCs is larger than  $R_e$  of FQGs. This systematic difference is expected because  $R_q$  is defined in a way different from  $R_e$ . We perform linear regression for the two relations and the results are also shown in Figure 7. For FQGs, we have  $\log R_{\text{FQG}}(M_*) = 0.79 \log M_*/M_\odot - 8.20$ . For QCCs, we have  $\log R_{\text{QCC}}(M_q) = 0.76 \log M_q/M_\odot - 7.54$ . The effective radius,  $R_e$ , of a QCC with  $M_q$  is defined as  $R_e(M_q) = R_q R_{\text{FQG}}(M_q)/R_{\text{QCC}}(M_q)$ . The underlying assumption in this definition is that QCCs have the same mass density profiles as FQGs of the same mass. Our examination shows that their surface mass density profiles are similar, and thus the assumption is valid. We then use the median  $\sigma$  of spaxels within  $0.2R_e$  to estimate the central velocity dispersion. For simplicity, the new central velocity dispersion is also denoted as  $\sigma_{\text{in}}$ .

Figure 8 shows  $\sigma_{\text{in}}$  versus  $M_q$  for QCCs. For comparison, we also show  $\sigma_{\text{in}}$  versus  $M_*$  for the corresponding PQGs in which QCCs are identified, and plot the QGSR to represent the result for FQGs. As expected, PQGs tend to lie below the QGSR, and the deviation from the QGSR increases with the decrease of  $\bar{f}_q$ . In contrast, most data points for QCCs follow closely the QGSR, with a few exceptions to be discussed in more detail in Section 4.3. We can quantify this by estimating the ‘distances’ of PQGs, QCCs and FQGs from the QGSR using a parameter defined as

$$\chi^2 = \frac{1}{N} \sum_{i=1}^N \frac{[\log \sigma_{\text{in},i} - \log \sigma_q(M_i)]^2}{e^2_{\sigma_{\text{in},i}} + \alpha^2 e^2_{M_i} + \Delta_q^2}, \quad (6)$$

where  $\alpha$  and  $\Delta_q$  are the slope and the intrinsic scatter of the QGSR,  $M_i$  is the  $M_*$  or  $M_q$  of the  $i$ th galaxy or

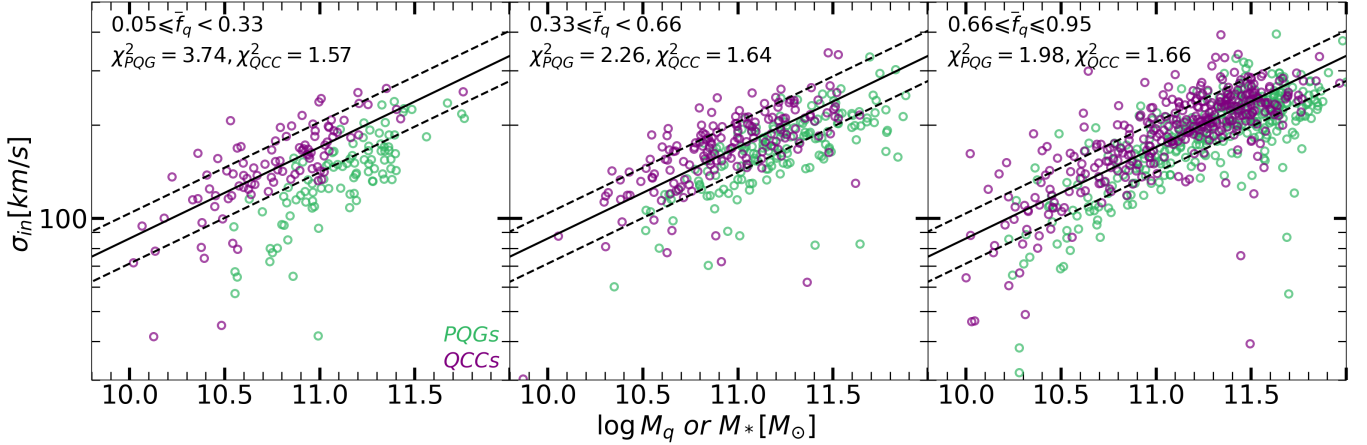


FIG. 8.— The  $\sigma_{\text{in}}$  versus  $M_q$  for QCCs (purple) and the  $\sigma_{\text{in}}$  versus  $M_*$  for PQGs in which QCCs are identified. The black solid lines show the QGSR (Equation 5) and dashed lines show the intrinsic scatter. We show galaxies in different  $\bar{f}_q$  bins in different panels. The parameters  $\chi^2$  presented in each panel are calculated using Equation 6 and show the distances of PQGs and QCCs to the QGSR. Please see the text for details.

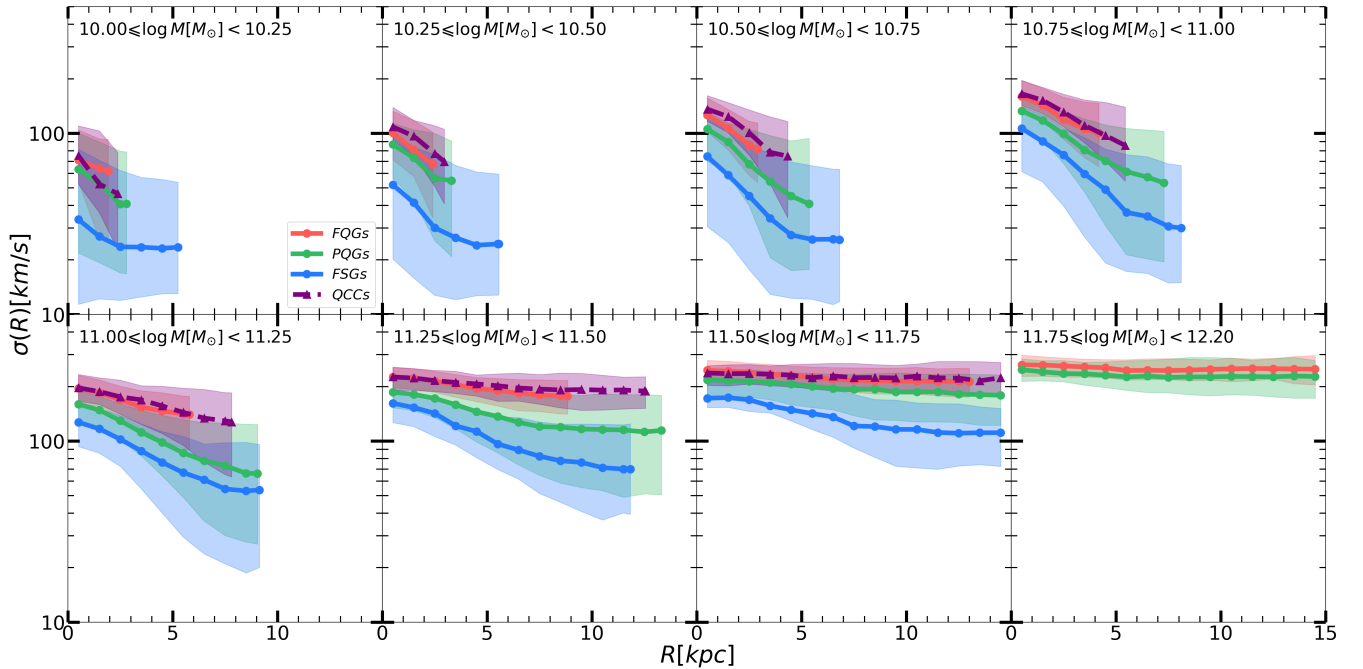


FIG. 9.— Stellar velocity dispersion ( $\sigma(R)$ ) profiles for FQGs (red), PQGs (green), FSGs (blue) and QCCs (purple). The solid and dashed lines show the median profiles of  $\sigma(R)$  while the shaded areas are the 16th and 84th percentiles. For galaxies, we show profiles up to the median of  $1.5R_e$ . For QCCs, we show the profiles to the median of  $R_q$ . The results for galaxies and objects with different mass are presented in different panels. We ignore the results if the number of galaxies or objects is less than 10.

QCC,  $\sigma_{\text{in},i}$  is  $\sigma_{\text{in}}$  of the  $i$ th object, and  $N$  is the number of objects. For FQGs, we obtain  $\chi_{\text{FQG}}^2 = 1.03$ . For galaxies with  $0.66 \leq \bar{f}_q \leq 0.95$ , we obtain  $\chi_{\text{PQG}}^2 = 1.98$  and  $\chi_{\text{QCC}}^2 = 1.66$ . For lower  $\bar{f}_q$ , the difference between QCCs and PQGs is even larger:  $\chi_{\text{PQG}}^2 = 2.26$  and  $\chi_{\text{QCC}}^2 = 1.64$  for  $0.33 \leq \bar{f}_q < 0.66$ ;  $\chi_{\text{PQG}}^2 = 3.74$  and  $\chi_{\text{QCC}}^2 = 1.57$  for  $0.05 \leq \bar{f}_q < 0.33$ . Note that the values of  $\chi_{\text{QCC}}^2$  are similar to  $\chi_{\text{FQG}}^2$ , quite independent of  $\bar{f}_q$ , while the values of  $\chi_{\text{PQG}}^2$  are significantly higher, especially for lower values of  $\bar{f}_q$ . This demonstrates clearly that quenched central cores are similar to fully quenched galaxies in that they are both dynamical hot for their stellar mass.

As mentioned in Section 2.3, we require  $R_q \geq R_{\text{th}} = 4''$  to identify QCCs. The PSF FWHM of MaNGA is about  $2''.5$ , which is expected to smooth both the quenching and  $\sigma$  profiles and to lead to some bias in the measurement. This effect may be particularly significant for  $M_q$  and  $R_q$  but should be weak for  $\sigma_{\text{in}}$ . This is because the quenching profile usually drops quickly around  $R_q$  (see Figure 2), while  $\sigma_{\text{in}}$  is measured in the central region where the profile is typically flat (see Figure 9). Our tests using different radius threshold,  $R_{\text{th}} = 2'', 3'', 4''$  and  $5''$ , confirm the smoothing effect. In general, QCCs defined using different  $R_{\text{th}}$  all follow a similar  $M_q$ - $\sigma_{\text{in}}$  relation close to the QGSR. However, using a smaller  $R_{\text{th}}$  leads to larger scatter in the relation and, on average,

gives slightly smaller  $M_q$  at given  $\sigma_{in}$ . The bias becomes insignificant when  $R_{th} \geq 4''$ . Note that QCCs can also be identified in FSGs of non-zero  $\bar{f}_q$  using smaller  $R_{th}$ , and they also follow the QGSR. However, they are excluded from our analyses because they do not meet the requirement that  $R_q \geq R_{th} = 4''$ .

In summary, the results presented in this section show that QCCs are similar to FQGs in that they are both dynamically hot (see also Section 3.4). This suggests that the relation between star formation quenching and dynamical hotness exists not only for galaxies but also for regions inside them. In this sense, a FQG can be considered as a QCC. As we will show below, this relation also holds in outer regions of galaxies, indicating that dynamical hotness is a necessary condition for quenching of star formation.

### 3.4. The Two- $\sigma$ diagram

To better understand the connection between quenching and dynamical hotness, we examine the velocity dispersion ( $\sigma$ ) profile and its connection to quenching. Figure 9 shows the median  $\sigma$  profiles for different populations of galaxies and for QCCs. The shaded regions cover 16th to 84th percentile of the distribution of individual profiles. As one can see, FQGs and QCCs are always similar and have the highest velocity dispersion profiles; FSGs have the lowest velocity dispersion and PQGs lie in between. For massive FQGs and QCCs,  $\sigma$  is almost independent of radius. A mild decline with radius can be seen in lower-mass objects. In contrast, FSGs, in particular those of  $\log M_*/M_\odot < 11$ , exhibit a transition in their profile: the velocity dispersion first decreases gradually with radius and then remains at a roughly constant level of about  $20 - 30 \text{ km s}^{-1}$  for low-mass galaxies and higher level for massive ones. All these indicate that dynamical hotness can vary within individual galaxies and the variation is systematically different for galaxies of different quenching properties. The difference between different populations appears to be larger in outer regions, in contrast to the fact that the stellar mass surface density profile in the outer region is quite similar for different populations (see Fang et al. 2013). This suggests that dynamical hotness may be more related to quenching than the local stellar mass surface density.

It is thus interesting to include the hotness in outer regions as an additional parameter to describe the dynamical properties of galaxies. Here we use  $\sigma_{out}$  defined in Section 2.2, and adopt its ratio with  $\sigma_{hot}$  to describe the outer hotness. In Figure 10, we show the Two- $\sigma$  diagram, which is  $\sigma_{out}/\sigma_{hot}(M_*)$  versus  $\sigma_{in}/\sigma_{hot}(M_*)$  for galaxies, and  $\sigma_{out}/\sigma_{hot}(M_q)$  versus  $\sigma_{in}/\sigma_{hot}(M_q)$  for QCCs. As one can see, FQGs occupy a small region around  $\log(\sigma_{in}/\sigma_{hot}) \sim 0$  and  $\log(\sigma_{out}/\sigma_{hot}) \sim -0.05$  with size  $0.1 \sim 0.2$  dex. Only a small fraction of FQGs have small  $\sigma_{out}/\sigma_{hot}$ . QCCs occupy almost the same region as FQGs, indicating that both QCCs and FQGs are dynamically hot in both inner and outer regions. PQGs are color-coded according to their  $\bar{f}_q$ . They have a narrow distribution in  $\sigma_{in}/\sigma_{hot}$ , with a median value slightly smaller than that of FQGs, but a much broad distribution in  $\sigma_{out}/\sigma_{hot}$ . They thus form a long vertical band extended to the region covered by FQGs. Along this vertical band with increasing  $\sigma_{out}/\sigma_{hot}$ , we can see an increasing trend of  $\bar{f}_q$  for PQGs accompanied by the

growth of their QCCs. It strongly suggests that the spreading of dynamical hotness tightly correlates with the spreading of quenching. Figure 5 shows that a small fraction of PQGs with  $\log sSFR < -12$  have almost the same  $\sigma_{in}$  distribution as FQGs. These galaxies occupy the same region as FQGs in Two- $\sigma$  diagram. FSGs have two branches, horizontal one and vertical one. Galaxies in the horizontal branch are all relatively cold in outer regions, while their inner regions can either be dynamically cold or hot. The vertical branch overlaps with the PQG band and also extends to the region covered by FQGs,

Comparing the Two- $\sigma$  diagram with Figure 4, we find that a significant fraction of PQGs and FSGs have smaller  $\sigma_{out}$  than FQGs, and so the Two- $\sigma$  diagram can be used to separate different populations of galaxies more effectively than the  $M_*$ - $\sigma_{in}$  diagram. For example, there are 1,073 FQGs, 484 PQGs and 130 FSGs enclosed by the circle of a radius of 0.15 dex, centered at (0,-0.05). Among the 484 PQGs, 255 of them have  $\log sSFR < -12$ . We find that about 71% of dynamically hot galaxies have  $\log sSFR < -12$  and 88% of hot galaxies have  $\log sSFR < -11$ . This clearly indicates a potential link between dynamical hotness and star formation quenching. In what follows, we use the Two- $\sigma$  diagram to define dynamic hotness of a whole object: an object is said to be dynamically hot when both  $\sigma_{in}$  and  $\sigma_{out}$  are close to the value of  $\sigma_{hot}$  corresponding to its stellar mass. Thus, both FQGs and QCCs are dynamically hot. Note that a small fraction of FSGs are also dynamically hot. This seems to suggest that dynamical hotness is a necessary, but not a sufficient condition for quenching. As we will discuss later, the existence of these hot star-forming objects suggests a potential path for galaxies to quench star formation.

The vertical band and horizontal branch represent the other two major dynamical status. The horizontal branch is dominated by FSGs, and only a few PQGs and FQGs are found in this branch. Galaxies on this branch have cold dynamics in both the inner and outer regions. The vertical band consists mainly of PQGs and FSGs. Galaxies in this band have relatively hot stellar component in the inner region but cold in the outskirts. The two dynamical status are roughly separated at  $\log(\sigma_{in}/\sigma_{hot}) \sim -0.3$ . As we will discuss in Section 4, the existence of well-defined branches of galaxy distribution in the Two- $\sigma$  diagram provides important clues about the coevolution between star formation in galaxies and their dynamical structure.

We also show the distributions of optically-selected AGNs, radio galaxies and barred galaxies (Section 2.1) in the lower panels of Figure 10. These three types of galaxies all have their specific regions of residence in the Two- $\sigma$  diagram. Both barred galaxies and optical AGNs reside on the vertical branch where PQGs are found, while radio galaxies can only be found in the top-right corner of the Two- $\sigma$  diagram where FQGs reside. All of these suggest a potential link among star formation quenching, AGN activities and feedback, and galaxy morphology and dynamical structure. We will come back to this issue in Section 4.

Measurements of velocity dispersion may be affected by rotation in edge-on galaxies. To check whether or not this has a significant impact on our results, we select galaxies with axis ratios  $b/a < 0.4$  and show them in the Two-

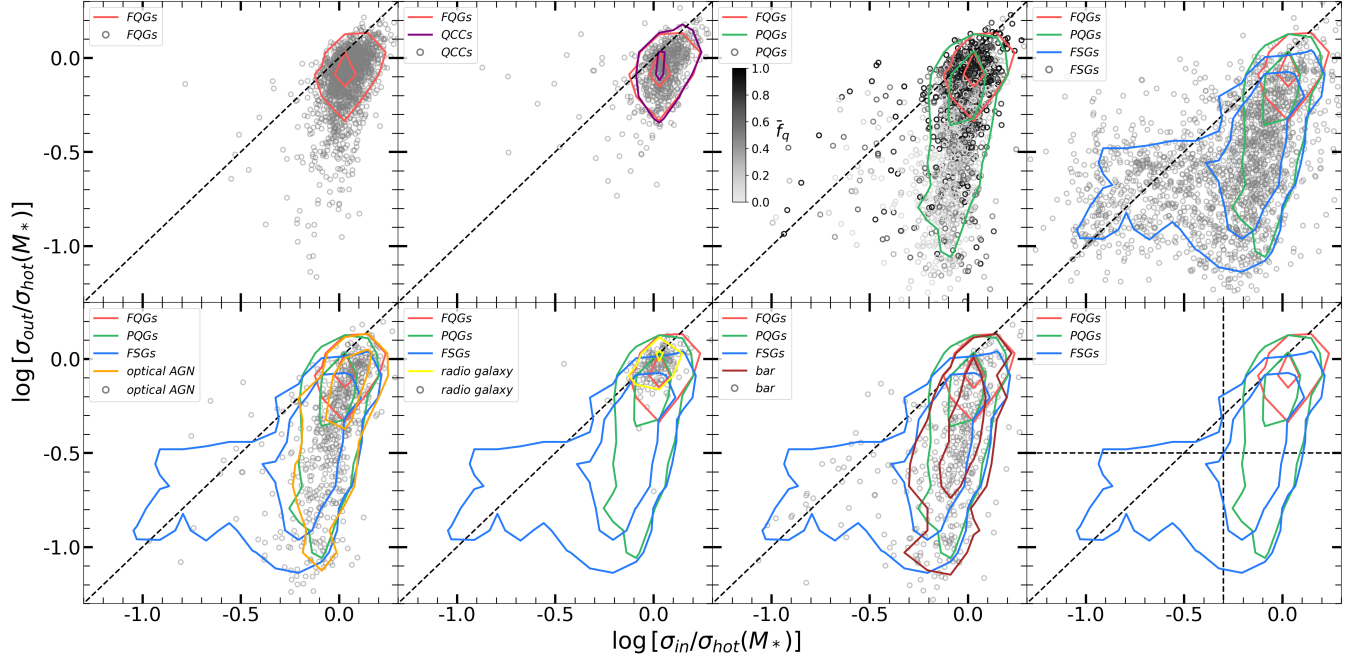


FIG. 10.— Two- $\sigma$  diagram:  $\sigma_{\text{out}}/\sigma_{\text{hot}}(M_*)$  versus  $\sigma_{\text{in}}/\sigma_{\text{hot}}(M_*)$ . For QCCs, it is  $\sigma_{\text{out}}/\sigma_{\text{hot}}(M_q)$  versus  $\sigma_{\text{in}}/\sigma_{\text{hot}}(M_q)$ . The small circles show the results for FQGs (upper-left), QCCs (upper-middle-left), PQGs (upper-middle-right), FSGs (upper-right), optical AGN host galaxies (lower-left), radio galaxies (lower-middle-left) and barred galaxies (lower-middle-right). In the upper-middle-right panel, PQGs are shown with color-coded circles according to their  $\bar{f}_q$ . In the lower-right panel, contour lines for FQGs (red), PQGs (green) and FSGs (blue) are shown. The inclined dashed lines show 1:1 relation. The horizontal and vertical dashed lines are the ones used to define horizontal and vertical sequences as discussed in Section 4. Contour lines with different colors correspond to different galaxies/objects as labeled in the corresponding panels. We show two contour levels, which enclose 40% and 80% of the galaxies/objects, respectively.

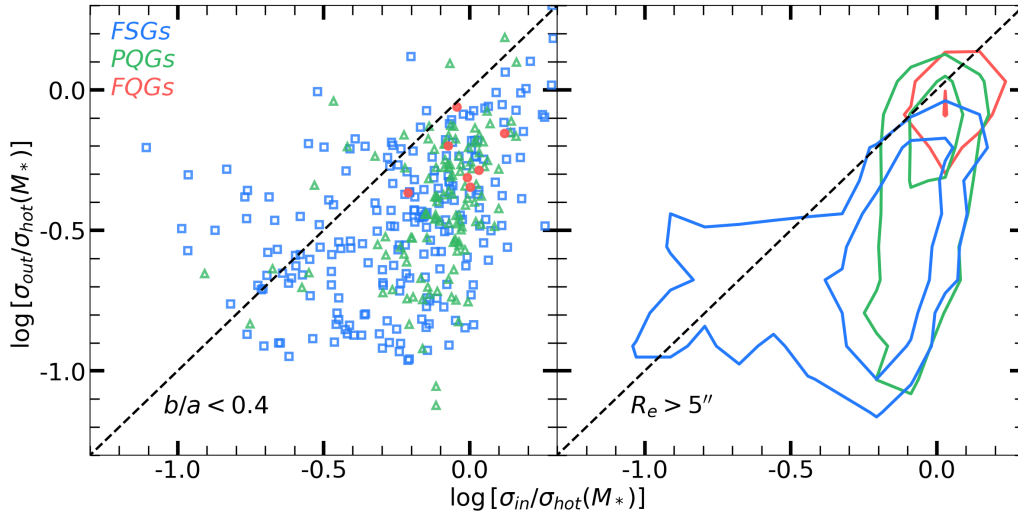


FIG. 11.— The left panel shows results for galaxies with  $b/a < 0.4$ . In the right panel,  $R_e$  is required to be greater than  $5''$ . Contour levels correspond to 40% and 80%. FQGs, PQGs and FSGs are in red, green and blue, respectively.

$\sigma$  diagram plotted in Figure 11. In the upper-left corner ( $\log(\sigma_{\text{out}}/\sigma_{\text{hot}}) > -0.5$  and  $\log(\sigma_{\text{in}}/\sigma_{\text{hot}}) < -0.4$ ), about 19% of FSGs have  $b/a < 0.4$ , significantly higher than the fraction for the total FSGs (12%). For PQGs, the fraction of edge-on galaxies is about 8% for the total population and about 14% in the upper-left corner. This suggests that the velocity dispersion of some galaxies in the upper-left corner is systematically overestimated because the rotation motion is not well subtracted. However, it is worthwhile noting that the majority of edge-on galaxies overlap with the main population in the Two- $\sigma$

diagram. This indicates that random motion and rotation can be well separated for most of edge-on galaxies.

If the angular size of a galaxy is comparable to the spaxel size ( $0''.5$ ), the measurement of  $\sigma$  may also be affected by rotation. To check this, we re-plot the Two- $\sigma$  diagram using galaxies with  $R_e > 5''$  in the right panel of Figure 11. The general trend does not change, but a significant fraction of FSGs around the dynamically hot systems now disappear. This indicates that the velocity dispersion of some of these FSGs is overestimated. Inspections of the images of these FSG galaxies showed that

some are indeed edge-on. However, adopting a cut in angular size can lead to severe bias. As shown in Section 4, FSGs with high  $\sigma_{\text{in}}$  and  $\sigma_{\text{out}}$  tend to have small physical sizes, and adopting a cut in the angular size will eliminate many of these compact galaxies, which may lead to bias. We thus do not apply such a cut in our analyses.

### 3.5. Other structural parameters

In the literature, many parameters have been used to characterize galaxy structure. These parameters can also be used to understand the connection between galaxy structure and star formation quenching. In this section, we present analyses similar to those shown in Section 3.2 for two additional structural parameters,  $\Sigma_1$  and Sérsic index  $n$ , as defined and measured in Section 2.2 and Section 2.1. We have also checked other parameters, such as the bulge-to-total mass ratio and profile concentration. The results are broadly consistent with those based on  $\sigma_{\text{in}}$ ,  $\Sigma_1$  and  $n$ , and are not shown here for brevity.

The first panel of Figure 12 shows  $\Sigma_1$  versus  $M_*$  for FQGs, PQGs and FSGs. Since QCCs are similar to FQGs, they are not shown here for clarity. In general,  $\Sigma_1$  increases with  $M_*$ . At given  $M_*$ , the surface density is the highest for FQGs and lowest for FSGs. These results are broadly consistent with those shown in Fang et al. (2013) and Barro et al. (2017). We find that the increasing trend appears to be reversed at  $\log M_*/M_\odot > 11.5$ , consistent with previous results (e.g. Graham & Guzmán 2003). This happens because the most massive elliptical galaxies have flattened cores. The quenched galaxies in Fang et al. (2013) and Barro et al. (2017) exhibit a stronger correlation between  $M_*$  and  $\Sigma_1$  than our FQGs because of different selection criteria used; they only considered galaxies with  $\log M_*/M_\odot < 11.5$ . We also show the relation between  $\Sigma_1$  and  $\sigma_{\text{in}}$  in the lower left panel. Consistent with Fang et al. (2013), the two quantities are tightly correlated with each other, and the correlation becomes weaker as  $\sigma_{\text{in}}$  decreases.

As shown in Barro et al. (2017), galaxy distribution in the  $\Sigma_1$ -sSFR plane also exhibit an L-shaped structure, suggesting that  $\Sigma_1$  is also a structural parameter that is closely related to star formation quenching. The reasons for us to adopt  $\sigma_{\text{in}}$  instead of  $\Sigma_1$  are the following. First, the L-shape structure in the  $\Sigma_1$ -sSFR diagram is looser, as shown by the low-redshift result in figure 6 of Barro et al. (2017), than that in the  $\sigma_{\text{in}}$ -sSFR diagram. Second, the correlation between  $\Sigma_1$  and  $M_*$  reverses at the massive end, as shown in Figure 12, which complicates the interpretation of the  $\Sigma_1$ -sSFR relation. Third, previous studies have shown that  $\sigma_{\text{in}}$  is more closely related to galaxy quenching than other structural parameters (e.g. Wake et al. 2012; Bluck et al. 2016, 2020a; Brownson et al. 2022). Fourth, as shown in Sections 3.4 and 4, the velocity dispersion can be used to separate galaxies of different dynamical status. Finally, it is more straightforward to connect velocity dispersion to supermassive black hole mass that is thought to be closely related to galaxy quenching (see Section 5).

Next, let us examine using the Sérsic index  $n$  as a structural parameter. This index is often used to describe the galaxy morphology and surface density profile. A galaxy with  $n = 1$  is a pure exponential disk, while  $n \geq 4$  is usually found for elliptical galaxies. The Sérsic indices used here were derived from the SDSS  $r$ -band im-

ages, taken from the NYU-VAGC catalog (Blanton et al. 2005). An upper limit of  $n = 6$  was set in the fitting. The upper right panel of Figure 12 shows  $n$  versus  $M_*$ . There is a loose correlation between the two quantities, with more massive galaxies tending to have higher  $n$ . Moreover, FQGs on average have higher  $n$  than FSGs at given  $M_*$ . We also present  $n$  versus  $\sigma_{\text{in}}/\sigma_{\text{hot}}$  in the lower right panel. Here one can see an L-shaped structure in the distribution. Most galaxies at  $\log(\sigma_{\text{in}}/\sigma_{\text{hot}}) < -0.3$  have  $n$  between 1 and 2, independent of  $\sigma_{\text{in}}/\sigma_{\text{hot}}$ . As  $\log(\sigma_{\text{in}}/\sigma_{\text{hot}}) > -0.3$ , the value of  $n$  ranges from 1 to 6. FQGs have a very broad  $n$  distribution and are mixed with other galaxies, indicating that it is difficult to use  $n$  to separate galaxies of different quenching status. We have also checked the relation between sSFR and  $n$ , and found a negative and loose correlation. No L-shaped structure is seen in the distribution of galaxies in the sSFR- $n$  plane.

## 4. CO-EVOLUTION OF DYNAMICAL STATUS AND STAR FORMATION

The Two- $\sigma$  diagram shows that galaxy distribution in this diagram is L-shaped. Here we investigate in more detail galaxy properties in this distribution by separating galaxies into two dynamical sequences (see the lower-right panel of Figure 10):

- *Horizontal sequence:* galaxies with  $\log(\sigma_{\text{out}}/\sigma_{\text{hot}}) < -0.5$ ;
- *Vertical sequence:* galaxies with  $\log(\sigma_{\text{in}}/\sigma_{\text{hot}}) > -0.3$ .

This separation roughly separates the two main components seen in the Two- $\sigma$  diagram. We note that the two sequences overlap in the lower-right corner. In the following, we investigate how galaxy structure and activity change along the two sequences. We will also examine galaxies outside the main sequences. The goal here is to understand how the dynamical and structural properties, star formation and nucleus activities are connected.

### 4.1. The horizontal sequence

Here we examine three structural parameters, Sérsic index  $n$ , galaxy size ( $R_e$ ) and the fraction of barred galaxies ( $f_{\text{bar}}$ ). The left panel of Figure 13 shows  $n$  as a function of  $\sigma_{\text{in}}/\sigma_{\text{hot}}$ . We can see that most of the galaxies with  $\log(\sigma_{\text{in}}/\sigma_{\text{hot}}) < -0.3$  have  $n$  between 1 and 2, quite independent of  $\sigma_{\text{in}}/\sigma_{\text{hot}}$ . Our visual inspections showed that most of these galaxies possess spiral arms, indicating that the horizontal sequence at  $\log(\sigma_{\text{in}}/\sigma_{\text{hot}}) < -0.3$  is dominated by disk galaxies. This is consistent with the small velocity dispersion observed in both inner and outer regions. At  $\log(\sigma_{\text{in}}/\sigma_{\text{hot}}) > -0.3$ , the value of  $n$  suddenly becomes much larger and has a much broader distribution, indicating that galaxies become more concentrated and diverse. The data thus suggests a morphological transition at  $\log(\sigma_{\text{in}}/\sigma_{\text{hot}}) \sim -0.3$ . Such a transition can also be seen in the other two structural parameters. The middle panel shows galaxy size ( $R_e$ ) as a function of  $\sigma_{\text{in}}/\sigma_{\text{hot}}$ . Here galaxy sizes are normalized by the best-fit  $M_*$ - $R_e$  relation for FQGs (see Figure 7). At  $\log(\sigma_{\text{in}}/\sigma_{\text{hot}}) < -0.3$ , galaxy size is almost independent of  $\sigma_{\text{in}}/\sigma_{\text{hot}}$ , while at  $\log(\sigma_{\text{in}}/\sigma_{\text{hot}}) > -0.3$

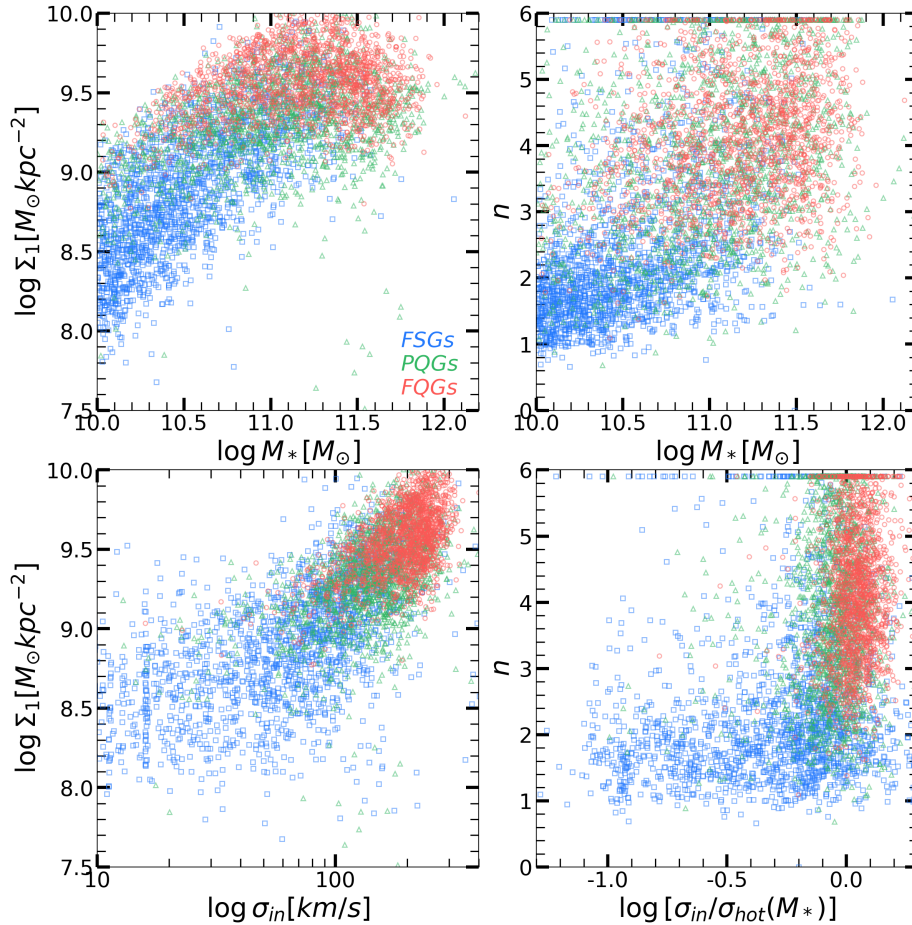


FIG. 12.— Top left panel:  $\Sigma_1$  versus stellar mass; top right panel: Sérsic index  $n$  (r band) versus stellar mass; bottom left panel:  $\Sigma_1$  versus  $\sigma_{in}$ ; bottom right panel: Sérsic index  $n$  versus  $\sigma_{in}/\sigma_{hot}(M_*)$ . FSGs, PQGs and FQGs are shown in blue squares, green triangles and red circles, respectively.

there is a sudden drop. This again suggests a transition to higher concentration, similar to that seen in  $n$ . The barred galaxy fraction,  $f_{bar}$ , is shown as a function of  $\sigma_{in}/\sigma_{hot}$  in the right panel. At  $\log(\sigma_{in}/\sigma_{hot}) < -0.3$ ,  $f_{bar}$  is almost a constant at a low value around 6%. But the fraction increases quickly at  $\log(\sigma_{in}/\sigma_{hot}) > -0.3$ , in particular for PQGs. This suggests that the presence of a bar is somehow linked to the dynamical hotness in the inner region of a galaxy (see also Figure 10).

In Figure 14, we show the sSFR as a function of  $\sigma_{in}/\sigma_{hot}$ . An L-shaped distribution, similar to that in Figure 5, can be clearly seen. At  $\log(\sigma_{in}/\sigma_{hot}) < -0.3$ , galaxies have  $\log \text{sSFR} \sim -10.2$ , independent of velocity dispersion. A quick drop in the sSFR occurs around  $\log(\sigma_{in}/\sigma_{hot}) \sim -0.3$ , and a large number of PQGs emerge above this value of  $\log(\sigma_{in}/\sigma_{hot})$ . This transition clearly indicates that quenching of central parts of galaxies occurs when the central parts become dynamically hot, although the whole galaxies are dynamically cold and star forming, as discussed in Section 3.3.

AGN feedback is thought to be one of the major mechanisms to quench star formation. It is thus interesting to examine the change of AGN activities along the horizontal sequence. The right panel of Figure 14 shows the fraction of optically selected AGNs,  $f_{AGN}$ , as a function of  $\sigma_{in}/\sigma_{hot}$ . Here again, we see a dramatic change in  $f_{AGN}$  at  $\log(\sigma_{in}/\sigma_{hot}) \sim -0.3$ . The fraction is very

low, usually less than 2%, at  $\log(\sigma_{in}/\sigma_{hot}) < -0.3$ . At  $\log(\sigma_{in}/\sigma_{hot}) > -0.3$ , the fraction can reach as high as 23% for the whole galaxy population. The jump is particularly large for PQGs, from zero to about 30%. The result is consistent with that shown in Figure 10. Given that the AGN duty cycle is typically  $10^8$  years (e.g. Marconi et al. 2004), the high AGN fraction suggests that almost all of the galaxies at  $\log(\sigma_{in}/\sigma_{hot}) > -0.3$  have gone through AGN phases in a few hundred-million years in the past.

To summarize, our results show that galaxy structure and activity make a fast transition along the horizontal sequence when the central velocity dispersion reaches about half of the velocity dispersion of a dynamically hot system according to their mass: galaxies become more concentrated, morphologically more diverse, with stronger bar and AGN activities as they cross the transition line. This transition also marks the onset of star-forming quenching in central regions of galaxies. All these indicate a close link of dynamical hotness with structural properties of galaxies, AGN feeding and star formation quenching. We will come back to this in Section 4.4.

#### 4.2. The vertical sequence

The left panel of Figure 15 shows the Sérsic index,  $n$ , as a function of  $\sigma_{out}/\sigma_{hot}$  along the vertical sequence

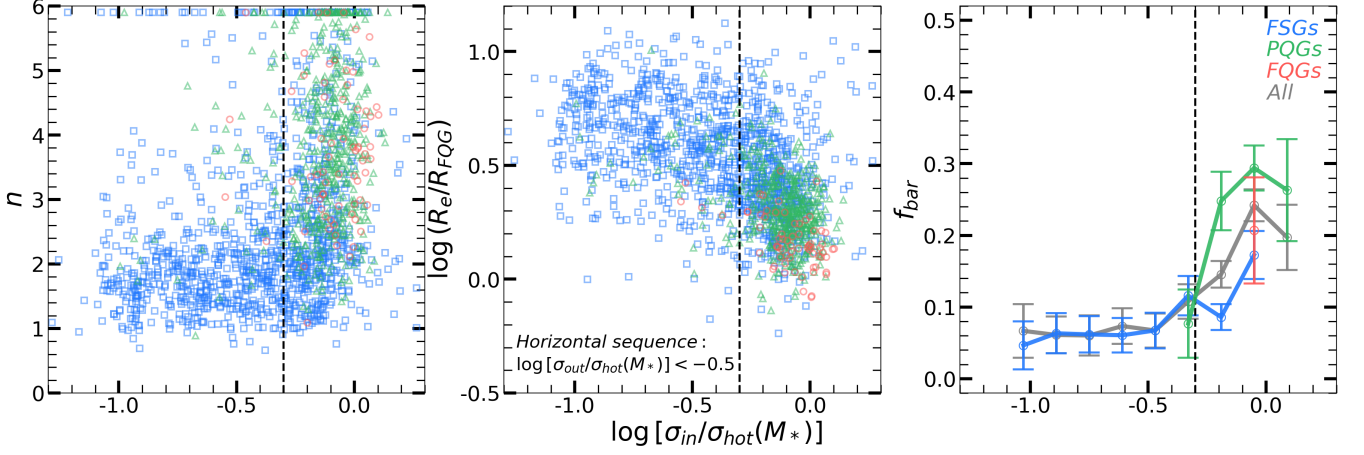


FIG. 13.— Galaxy structure along horizontal sequence ( $\log(\sigma_{\text{out}}/\sigma_{\text{hot}}) < -0.5$ ). FSGs, PQGs and FQGs are shown in blue, green and red, respectively. Left panel: Sérsic index  $n$  as a function of  $\log(\sigma_{\text{in}}/\sigma_{\text{hot}})$ . Middle panel:  $\log[R_e/R_{\text{FQG}}(M_*)]$  as a function of  $\log(\sigma_{\text{in}}/\sigma_{\text{hot}})$ , where  $R_{\text{FQG}}(M_*)$  is the best fitting for the mass-size relation of FQGs shown in Figure 7. Right panel: Barred galaxy fraction ( $f_{\text{bar}}$ ) as a function of  $\log(\sigma_{\text{in}}/\sigma_{\text{hot}})$ . Gray line shows the results for all galaxies and error bars are obtained with bootstrap method. The vertical dashed lines show  $\log(\sigma_{\text{in}}/\sigma_{\text{hot}}) = -0.3$ . We do not show the results in bins with galaxy number less than 20.

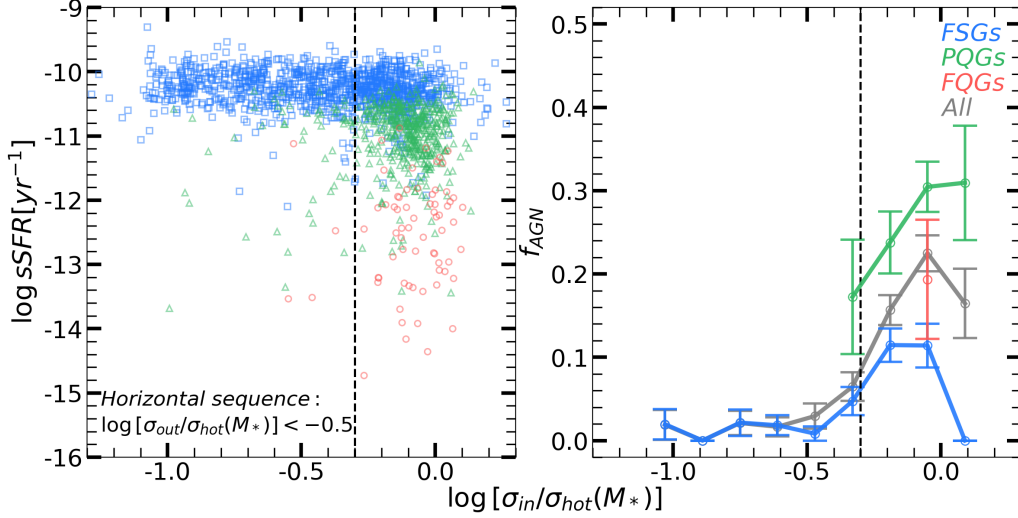


FIG. 14.— Galaxy activity along the horizontal sequence ( $\log(\sigma_{\text{out}}/\sigma_{\text{hot}}) < -0.5$ ). FSGs, PQGs and FQGs are shown in blue, green and red, respectively. Left panel: sSFR as a function of  $\log(\sigma_{\text{in}}/\sigma_{\text{hot}})$ . Right panel: Similar to the right panel of Figure 13 but for optical AGN fraction ( $f_{\text{AGN}}$ ) as a function of  $\log(\sigma_{\text{in}}/\sigma_{\text{hot}})$ . The vertical dashed lines show  $\log(\sigma_{\text{in}}/\sigma_{\text{hot}}) = -0.3$ .

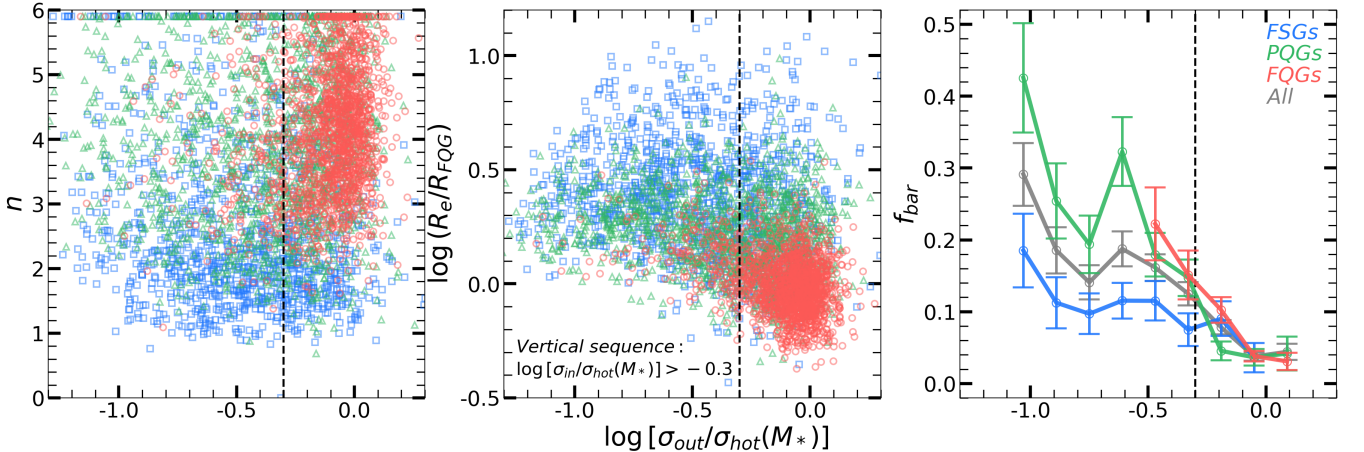


FIG. 15.— Similar to Figure 13 but here we show the structural parameters for galaxies along the vertical sequence ( $\log(\sigma_{\text{in}}/\sigma_{\text{hot}}) > -0.3$ ) as functions of  $\log(\sigma_{\text{out}}/\sigma_{\text{hot}})$ . The vertical dashed lines show  $\log \sigma_{\text{out}}/\sigma_{\text{hot}} = -0.3$ .

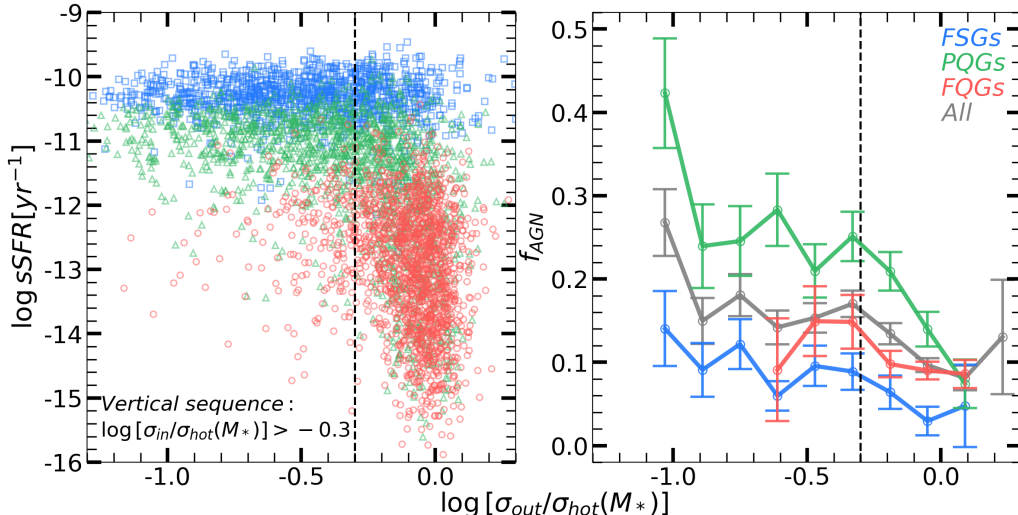


FIG. 16.— Similar to Figure 14 but here we show sSFR and  $f_{\text{AGN}}$  for galaxies along the vertical sequence ( $\log(\sigma_{\text{in}}/\sigma_{\text{hot}}) > -0.3$ ) as functions of  $\log(\sigma_{\text{out}}/\sigma_{\text{hot}})$ . The vertical dashed lines show  $\log(\sigma_{\text{out}}/\sigma_{\text{hot}}) = -0.3$ .

defined above. In general, all the three populations of galaxies, FSGs, PQGs and FQGs, have very broad distributions in  $n$ , indicating that galaxies in this sequence have diverse morphology. For a given population, there is no significant dependence of  $n$  on  $\sigma_{\text{out}}/\sigma_{\text{hot}}$ , although different populations are distributed differently. The middle panel shows  $R_e/R_{\text{FQG}}(M_*)$  as a function of  $\sigma_{\text{out}}/\sigma_{\text{hot}}$ . The size ratio decreases with increasing  $\sigma_{\text{out}}/\sigma_{\text{hot}}$ , and the trends for PQGs and FSGs are similar. The right panel shows that the fraction of barred galaxies gradually declines from 30% to 4% as  $\sigma_{\text{out}}/\sigma_{\text{hot}}$  increases from  $\sim 0.1$  to  $\sim 1$ , and the trend exists for all the three populations, being the strongest for PQGs. Combining these results with those for the horizontal sequence, we can conclude that galaxy bars prefer to live in galaxies located in the lower-right corner of the Two- $\sigma$  diagram, where a galaxy is dynamically hot in the central region but cold in the outskirts.

Figure 15 shows that a fraction of FSGs have sizes larger than those of PQGs of the same mass. To understand the difference, we selected FSGs with  $\log(R_e/R_{\text{FQG}}) > 0.6$  and checked their properties. Most of these galaxies have  $n$  between 1 and 2, suggesting that they are spiral galaxies. In comparison, PQGs usually have  $n > 2$  (see the left panel). In the Two- $\sigma$  diagram, FSGs tend to be located closer to the limit of the vertical sequence at  $\log(\sigma_{\text{in}}/\sigma_{\text{hot}}) = -0.3$  than PQGs. This suggests that the difference between FSGs and PQGs may be mainly in their  $\sigma_{\text{in}}$  distribution.

The left panel of Figure 16 shows the sSFR versus  $\sigma_{\text{out}}/\sigma_{\text{hot}}$ . FSGs have almost constant sSFR, independent of  $\sigma_{\text{out}}/\sigma_{\text{hot}}$ , similar to that along the horizontal sequence. The independence of the lower bound of sSFR is caused by the D4000 threshold used to define FSGs, but the presence of the roughly constant upper bound in sSFR indicates that there is an upper limit of sSFR that is quite independent of dynamical hotness. The sSFR of PQGs appears to be lower than that of FSGs, as expected from their definition, and decreases gradually with increasing  $\sigma_{\text{out}}/\sigma_{\text{hot}}$  at  $\log(\sigma_{\text{out}}/\sigma_{\text{hot}}) < -0.3$ . It is consistent with the increasing trend of  $\bar{f}(q)$  with increasing  $\sigma_{\text{out}}/\sigma_{\text{hot}}$  shown in Figure 10. At  $\log(\sigma_{\text{out}}/\sigma_{\text{hot}}) \sim -0.3$ ,

however, the sSFR drops quickly and the FQG population emerges. The overall distribution of galaxies is L-shaped. This demonstrates that the L-shaped distribution shown in Figure 5 contains two transitions. The first occurs when the central region of a galaxy becomes dynamically hot, i.e. when  $\log(\sigma_{\text{in}}/\sigma_{\text{hot}})$  reaches  $-0.3$  (Figure 14). This corresponds to the emergence of PQGs and QCCs. The second transition occurs when a galaxy becomes dynamically hot over its entire body, i.e. when  $\log(\sigma_{\text{out}}/\sigma_{\text{hot}})$  reaches  $\sim -0.3$  (Figure 16). This corresponds to the emergence of the FQG population. Note, however, when considered as systems of their own mass, QCCs occupy the same region as FQCs, which implies that the presence of a dynamically cold component in the outer part of a galaxy does not have a strong impact on the inner hot component.

Optical AGNs reside throughout the vertical sequence (Figure 10). We show the fraction of optical AGNs along the vertical sequence in the right panel of Figure 16. The fraction is the highest for PQGs and the lowest for FSGs. The optical AGN fraction declines as  $\sigma_{\text{out}}/\sigma_{\text{hot}}$  increases, and the decline becomes stronger at  $\log(\sigma_{\text{out}}/\sigma_{\text{hot}}) > -0.3$ . Combining these results with the corresponding results for the horizontal sequence, we can see that optical AGNs are preferentially found in galaxies located in the lower-right corner of the Two- $\sigma$  diagram. This is similar to the fraction of barred galaxies, suggesting a potential connection between these two populations of galaxies. Radio galaxies, which are also referred to as AGNs, are all dynamically hot, which is consistent with their hosts being elliptical galaxies. Most (151/156) of our radio galaxies are classified as low-excitation radio mode and most of them have  $\log M_*/M_\odot > 11$ , indicating that they might be powered by Bondi accretion of hot gas. Almost no radio galaxy is found to be dynamically hot in the central region and cold in the outskirts, indicating the presence of a radio AGN is very sensitive to the dynamical state even in the outer part of its host.

Images of dynamically hot galaxies may provide additional information about underlying processes relevant to the observed connection of galaxy properties. We thus selected galaxies within a circle of radius of 0.15 dex,



centered at (0,-0.05), in the Two- $\sigma$  diagram. Most of the FQGs and PQGs in this region appear to be round and smooth, consistent with being dynamically hot. FSGs in this region usually appear to be compact, with sizes comparable to those of the FQGs of the same mass. We inspected the SDSS images of these galaxies and found that some FSGs appear to be edge-on spirals. However, the fraction of FSGs with  $b/a < 0.4$  is only about 12%, comparable to the FSG population located outside the region. About 20% of the FSGs in this region show spiral arms, and most of the spiral arms appear asymmetric. More interestingly, more than half of FSGs in this region show significant asymmetric, sometimes clumpy, structures. These hot FSGs thus appear to have experienced significant interactions and/or mergers in the recent past.

A small fraction of galaxies in the vertical sequence have very large central velocity dispersion (Figure 10). We selected galaxies with  $\log \sigma_{\text{in}} \geq \log \sigma_{\text{q}}(M_*) + 3\Delta_{\text{q}}$ , which gave 3 FQGs, 6 PQGs and 22 FSGs. We inspected the 22 images of FSGs and found that only four are regular, edge-on disks. The large  $\sigma_{\text{in}}$  for these disk galaxies is caused by rotation. The rest FSGs all exhibit clear signature for galaxy interaction and/or merger, showing close companions, asymmetric structure and tidal tails. The violent interaction can significantly increase the random motion of stars, making a system dynamically hot. Indeed, as shown by some recent simulations (see e.g. Sotillo-Ramos et al. 2022), newly-born stars during merger tend to have chaotic orbits. This might explain why this sub-population is dominated by FSGs.

Among the interacting FSGs, three galaxies, MaNGA-9182-9102, MaNGA-8937-3703 and MaNGA-8248-6104, are particularly interesting. They are identified as FSGs (based on D4000) but have very low star formation rate ( $\log \text{sSFR} < -12$ ). Two of them can be found in the upper-third and the lower-second panels of Figure 5, respectively. The third one has  $\log(\sigma_{\text{in}}/\sigma_{\text{hot}}) = 0.69$  and thus lies outside of the boundary of the figure. These galaxies have small D4000 over the entire galaxies, implying that they are young, but their current specific star formation rates are low. This may suggest that their star formation is quenched recently by a fast process associated with a recent violent interaction. These three galaxies will evolve leftwards in the Two- $\sigma$  diagram as they relax to dynamical equilibrium, eventually joining the FQG population.

#### 4.3. Outliers

In the two lowest stellar mass bins, some FQGs and PQGs are located far from the dominating L-shape distribution in the sSFR- $\sigma_{\text{in}}$  plane (Figure 5). They have small  $\sigma_{\text{in}}$  and low sSFR. In addition, a small fraction of FQGs have  $\sigma_{\text{out}}$  significantly lower than the main population (Figure 10). The significance of the presence of these outliers is difficult to evaluate. One possibility is that these galaxies are disk-like, but they are satellite galaxies or splash back galaxies that have been strongly quenched by environmental processes. The satellite fraction decreases with increasing stellar mass, and so this possibility is higher for galaxies of lower mass. This is consistent with the fact that these galaxies have relatively low stellar mass, as can be seen in Figure 5. However, some of these galaxies are massive, with  $M_* \sim 10^{11} M_{\odot}$ , for which environmental effects are expected to be weak (e.g. Peng

et al. 2010; Li et al. 2020). Some other processes may be responsible for quenching such massive and cold galaxies.

Figure 8 shows that some QCCs have very low  $\sigma_{\text{in}}$  (see also Figure 10). There are in total 27 QCCs with  $\log \sigma_{\text{in}} < \log \sigma_{\text{q}}(M_{\text{q}}) - 2\Delta_{\text{q}}$ . We checked their  $\sigma$  profiles and found that 17 of them exhibit a clear drop of  $\sigma$  in the inner region. The upper-right panel in Figure 10 shows that a small fraction of PQGs have smaller  $\sigma_{\text{in}}$  than the main population. We also checked their  $\sigma$  profiles and found that about 60% of them show a clear drop of  $\sigma$  in the inner region. We also checked the  $\sigma$  profiles of FSGs with  $\log(\sigma_{\text{out}}/\sigma_{\text{hot}}) > -0.4$  and  $\log(\sigma_{\text{in}}/\sigma_{\text{hot}}) < -0.5$ , and found a similar drop in the central region. This is not observed in normal galaxies, including FQGs, where the velocity dispersion almost always declines gradually with radius. More investigation is needed to understand the cause of the drop of  $\sigma$  in the inner regions of these galaxies.

#### 4.4. Evolutionary paths and jumps to dynamical hotness and quenching

The Two- $\sigma$ , sSFR- $\sigma_{\text{in}}$  and sSFR- $\sigma_{\text{out}}$  diagrams provide information about the co-evolution of galaxy star formation and dynamical structure. Here we use the Two- $\sigma$  diagram to illustrate these evolutionary paths, as shown in Figure 17. We emphasize that our discussion makes the assumption that the cosmic evolution of these diagrams is not large. This assumption has some observational support. As shown in Barro et al. (2017), the sSFR- $\Sigma_1$  diagram is almost the same for galaxies at different redshift. However, the evolution of the Two- $\sigma$  diagram is unknown. Moreover, the evolutionary paths shown in Figure 17, and discussed below only represent average trends; the paths taken by individual galaxies may be more complicated.

We envisage two major evolutionary paths. The first one is represented by the horizontal light-blue arrow, and corresponds to the horizontal sequence in the Two- $\sigma$  diagram. To the left, the galaxy population is dominated by star-forming disks, as shown by the representative galaxies in Figure 17. These disk galaxies may grow by gas accretion and star formation. The stellar surface density in the inner region may increase because of secular evolution and accretion of gas clouds. These galaxies maintain disk morphology and are relatively cold in the inner part, as long as the mass of the accreted material is insufficient to make the inner part hot. This process may lead to increases in the central velocity dispersion while the outer part remains dynamically cold. Bar and AGN activities may develop, but only at a low level in most of the galaxies, because most of the gas component in the inner part is still supported by angular momentum. Star formation can continue, as feedback is too weak to quench star formation even in the inner part. A galaxy can continue to evolve in this way until its central velocity dispersion reaches about half of  $\sigma_{\text{hot}}(M_*)$ .

A galaxy can become centrally hot when it is significantly disturbed, most likely by merger and interaction events that can cause significant loss of angular momentum in stars and gas clouds. If only minor mergers are involved, only the central part of a galaxy can be affected. The loss of angular momentum allows formed stars and gas clouds to sink toward the central region, making the galaxy more concentrated. If the merger is gas rich, star

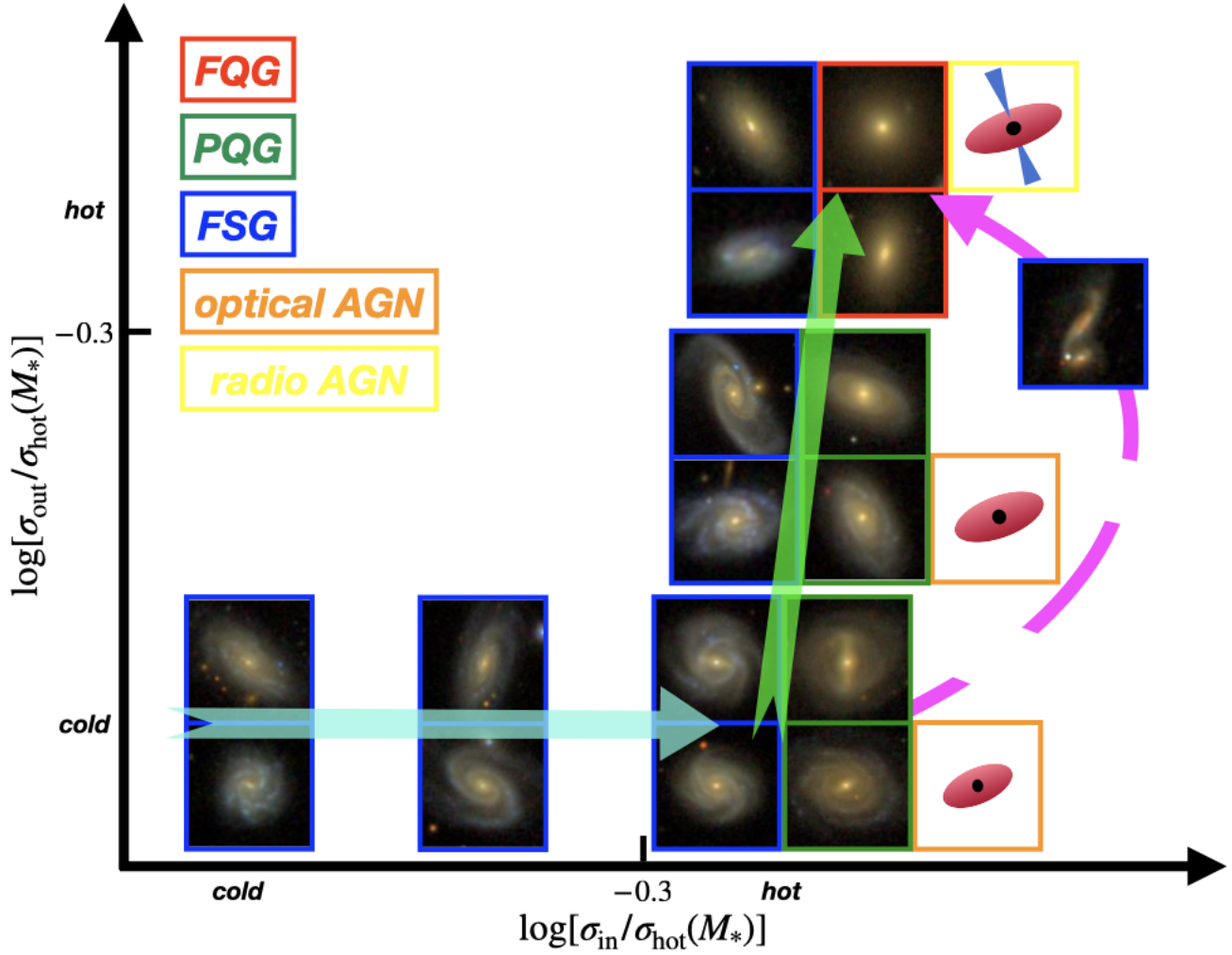


FIG. 17.— Schematic Two- $\sigma$  diagram. The arrows illustrate possible evolutionary tracks (see text for details). We also show the SDSS images of several representative galaxies located at different places along the horizontal and vertical sequences. Red, green and blue square frames indicate the images for FQGs, PQGs and FSGs, respectively. The orange and yellow frames indicate the sketches for optical and radio AGNs.

bursts and AGN activities can be triggered, and the associated feedback can start to affect the gas component and suppress star formation. The coexistence of FSGs and PQGs in the lower-right corner of the Two- $\sigma$  diagram suggests that either AGNs can be triggered only in some, but not all, galaxies, or some galaxies can regain cold gas supply in the dynamically hot region to offset the feedback. For PQGs where quenching has already occurred in the inner part, feedback should be effective only in the dynamically hot part, as most of the QCCs are dynamically hot. Physically, this may suggest that feedback is more effective in a more isotropic distribution of gas clouds than in a rotationally supported disk, as shown in simulations (e.g. Wagner et al. 2013). Together, the processes described above produced the first L-shaped distribution shown in the left panel of Figure 14.

Centrally hot galaxies in the lower right corner can evolve upwards, as indicated by the vertical green arrow in Figure 17. As shown in Figure 15, galaxies gradually shrink along this sequence, which may be caused by a compaction process similar to that discussed in Barro et al. (2017). If the compaction of a galaxy is due to

angular momentum loss produced by interactions and mergers, the orbits of stars and star-forming clouds can be randomized, making the galaxy hotter. Since the central region is already hot, i.e. already dominated by random motion, the effect is expected to be more important in the outer region where stars and gas clouds were still in a rotationally supported disk. This makes the galaxy move almost vertically in the Two- $\sigma$  diagram. However, for a galaxy where  $\sigma_{\text{in}}$  is still significantly lower than  $\sigma_{\text{hot}}(M_*)$ , the inner part can be ‘heated’ further so that the galaxy can move rightwards within the vertical sequence. As long as  $\log[\sigma_{\text{out}}/\sigma_{\text{hot}}(M_*)] < -0.3$ , most galaxies will remain as FSGs and PQGs. During the process, gas clouds that have lost rotational support can sink toward the center of a galaxy to feed the central black hole. AGN feedback may then expel the gas in the hot core, suppressing and eventually quenching star formation there. Meanwhile, star formation outside the hot core will continue as the feedback is not effective in affecting the gas in the disk. For some galaxies, quenching may not be important as their  $\sigma_{\text{out}}$  increases and their sizes shrink. These galaxies, which remain star forming, although dynamically hot, may be observed as blue com-

pact galaxies which are as dynamically hot as FQGs (see e.g. Barro et al. 2017).

When the total effect of galaxy interaction and merging is sufficiently strong, a galaxy will become dynamically hot over its entire body, and moves to the top right corner in the Two- $\sigma$  diagram (see the representative galaxies in this region in Figure 17). During this process, the gas over the entire galaxy can be affected by feedback effects. These galaxies will then become fully quenched quickly as strong AGN feedback expels gas out of galaxies, or slowly as star formation consumes cold gas. The fact that FQGs and QCCs are all dynamically hot indicates that quenching of star formation is effective only in a dynamically hot system.

Massive dynamically hot galaxies are usually surrounded by hot gas halos. Accretion of hot gas by the central SMBH can ignite ‘low-excitation’ radio AGNs (Best & Heckman 2012). These radio galaxies can heat the circum-galactic medium through radio-mode feedback (e.g. Croton et al. 2006), and prevent gas cooling and further star formation. These galaxies can thus become and remain as quenched galaxies. Low-mass dynamically hot galaxies may have a different fate: it may become totally quenched if no new star-forming gas is available or can maintain their star formation if they can acquire new gas. If the halo is not massive, cooling of the circum-galactic medium may occur, adding cold gas in the outskirts and forming a new disk. In this case, the galaxy may return to the PQG population. On the other hand, for a low-mass galaxy living in a dense environment, the surrounding gas may be too hot or moving too fast for it to capture, and the galaxy will eventually become fully quenched. This is consistent with the fact that dynamically hot, low-mass galaxies are diverse in their star formation. This suggests again that being dynamically hot is only a necessary, but not sufficient condition for star formation quenching.

The evolution along the horizontal and vertical sequences described above may occur in two different ways. The first is through some secular processes, such as the ones driven by bars and minor interactions. As shown in Figure 10 (see also the representative galaxies in 17), most of the barred galaxies lie along the vertical sequence, suggesting that bar-driven processes may be able to re-distribute gas and stars, making galaxies centrally hot. Bar-driven processes may also help trigger AGN activity, thereby affecting star formation. A recent investigation based on weak lensing and two-point correlation analyses (Zhang et al. 2021) provides some evidence for the role of minor interactions in triggering AGNs and building central mass concentration. They found that optically selected AGNs and star-forming galaxies of the same mass reside in halos of similar mass, but that AGNs are surrounded by more satellites. Furthermore, they also found that galaxies with larger central velocity dispersion tend to have more satellites. These results suggest that interactions with satellites may play an important role not only in dynamically ‘heating’ galaxies, but also in triggering AGNs and associated feedback. The second way is through violent interactions that make jumps along the two sequences in the Two- $\sigma$  diagram. There is evidence for strong interactions produced by major mergers in our sample of galaxies (see Section 4.2). Such a violent process can significantly enhance

dynamical hotness of galaxies and make a dynamically cold galaxy completely hot. Such interactions can also trigger strong AGNs, and the associated feedback may heat and/or expel gas effectively, quenching current star formation in galaxies. The associated process is expected to be fast and lead to jumps in the Two- $\sigma$  diagram, as represented schematically by the pink dashed arrow in Figure 17.

## 5. CONNECTION TO SUPERMASSIVE BLACK HOLES

As discussed above, our results indicate that AGN activities are related to dynamical hotness of their host galaxies. Given that AGN feedback, which has been considered as one of the main processes of star formation quenching (e.g. Silk & Rees 1998; Croton et al. 2006; Heckman & Best 2014), is driven by the accretion of supermassive black holes (SMBHs), it is interesting to investigate how the growth of SMBH fits in the evolutionary scenario proposed above. In this section, we present more analyses along this line. In particular, we propose that the formation of dynamically hot systems, the growth of SMBHs and quenching of star formation are all closely related.

### 5.1. A simple model

Let us consider a gas/star system with a given total mass. At any given time, the supermassive black hole mass is  $M_{\text{BH}}$  and the stellar mass is  $M_*$ . We write the total energy released by the accretion of the SMBH as  $E = \epsilon M_{\text{BH}} c^2 / (1 - \epsilon)$ , where  $\epsilon$  is the mass-to-energy efficiency and  $c$  is the speed of light. Only a fraction of the energy is expected to be coupled with the inter-stellar medium (ISM) to prevent it from forming stars either by ejecting the gas or by keeping the gas hot. Denoting this fraction as  $f_{\text{cp}}$ , we can write the total gas mass that a SMBH prevents from turning into stars as

$$M_{\text{gas}} = \frac{f_{\text{cp}} \epsilon M_{\text{BH}} c^2}{1/2(1 - \epsilon)v_{\text{esc}}^2} = \frac{2\epsilon f_{\text{cp}} M_{\text{BH}} c^2}{(1 - \epsilon)a^2 \sigma_{\text{in}}^2}, \quad (7)$$

where  $v_{\text{esc}}$  is the escape velocity. Since  $v_{\text{esc}}$  is directly related to the gravitational potential of the galaxy, we assume that  $v_{\text{esc}} = a\sigma_{\text{in}}$ . The SMBH continues to grow its mass until most of gas in the host galaxy is affected by the feedback and star formation is also quenched. We write the gas-to-star mass ratio as  $f_{\text{gas}} = M_{\text{gas}}/M_*$ . The SMBH mass in the quenched object (galaxy or QCC) can then be written as

$$M_{\text{BH}} = \frac{(1 - \epsilon)a^2 f_{\text{gas}} M_* \sigma_{\text{in}}^2}{2\epsilon f_{\text{cp}} c^2} = \gamma M_* \sigma_{\text{in}}^2, \quad (8)$$

where  $\gamma \equiv (1 - \epsilon)a^2 f_{\text{gas}} / 2\epsilon f_{\text{cp}} c^2$ .

As shown in Section 3, most quenched objects (FQGs and QCCs) are dynamically hot. Thus, the above relation is expected to be valid only for dynamically hot systems where  $\sigma_{\text{in}} \approx \sigma_{\text{hot}}(M_*)$ . As one can see, if  $\gamma$  is roughly a constant, the above relation, combined with the  $\sigma_{\text{in}}-M_*$  relation (i.e. quenched galaxy scaling relation), leads to a relation between  $M_{\text{BH}}$  and  $\sigma_{\text{in}}$ , or between  $M_{\text{BH}}$  and  $M_*$ . This suggests that we can use the observed scaling relations of  $M_{\text{BH}}$  with  $M_*$  and  $\sigma_{\text{in}}$  to constrain  $\gamma$ . For this purpose, we combine the QGSR

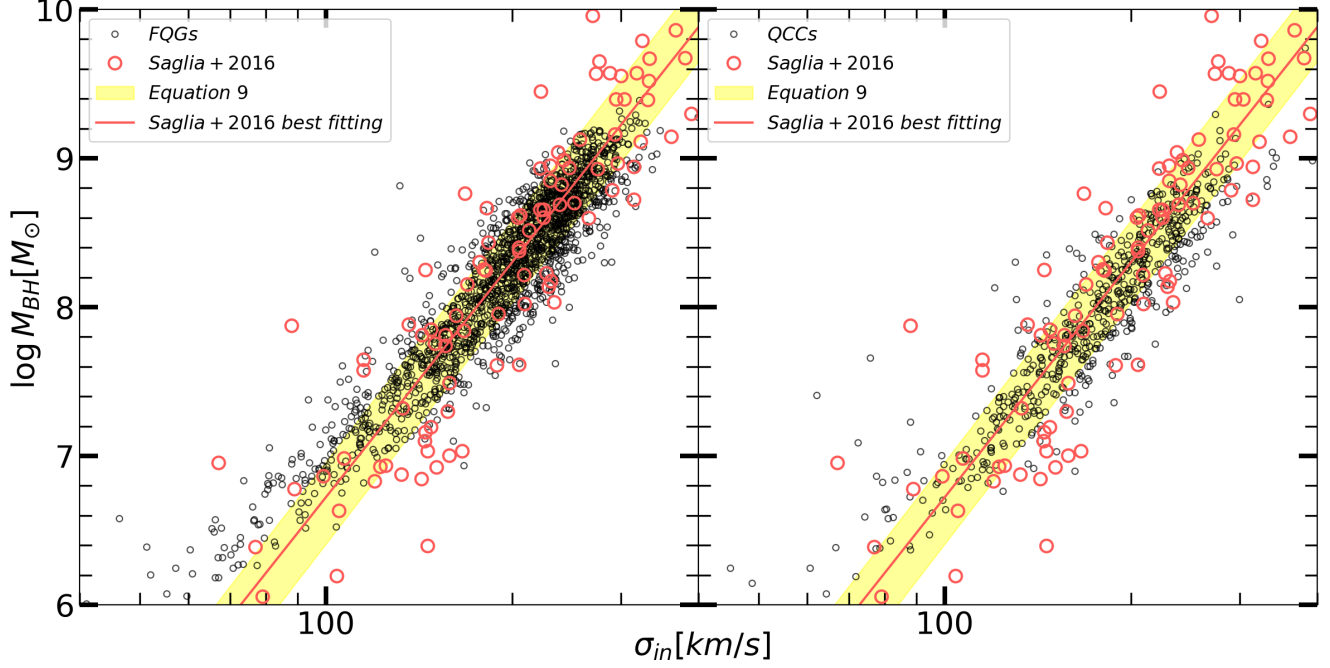


FIG. 18.— The black circles show the predicted  $M_{\text{BH}}$  versus  $\sigma_{\text{in}}$  for FQGs (left) and QCCs (right). The  $M_{\text{BH}}$  is calculated using Equation 8. The yellow bands show the predicted  $M_{\text{BH}}-\sigma_{\text{in}}$  relation (Equation 9) and its one- $\Delta$  uncertainty based on the best-fitting of the QGSR. The red circles show the observational data (BH1 sample) with dynamically measured black hole masses, taken from Saglia et al. (2016). The solid red lines show the best-fitting of the BH1 sample, also taken from Saglia et al. (2016).

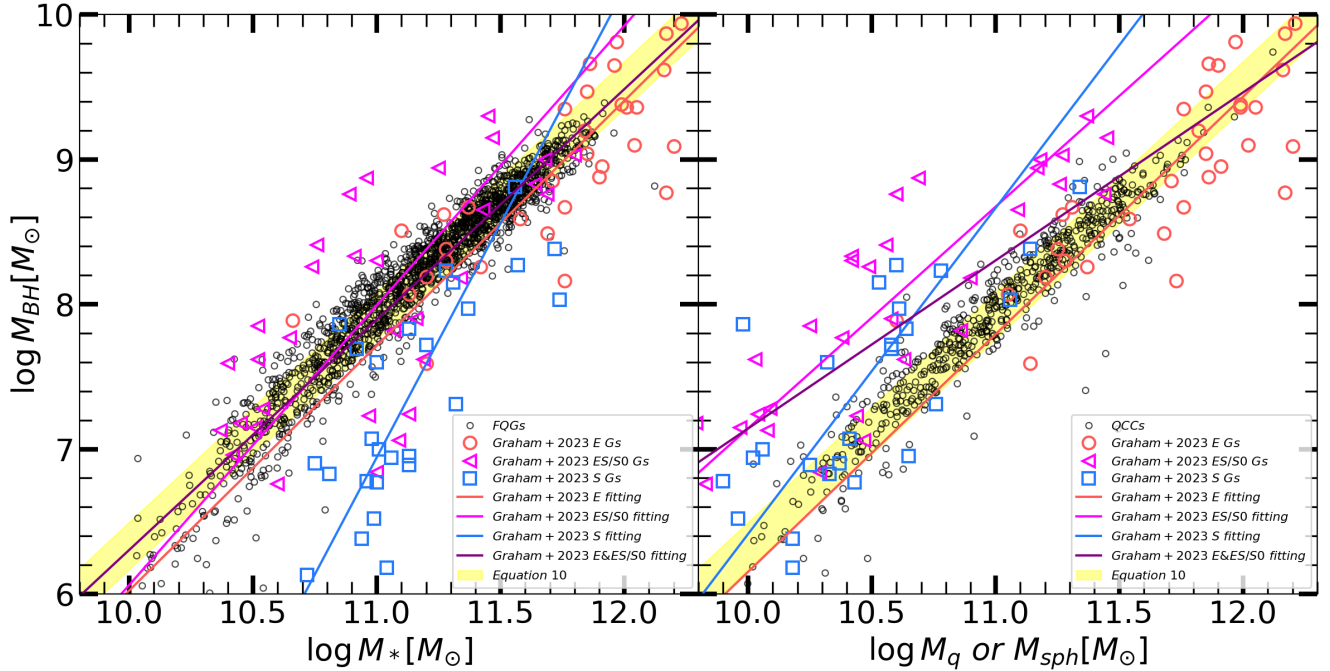


FIG. 19.— The black circles show the predicted  $M_{\text{BH}}$  versus  $M_*$  relation for FQGs (left) and the predicted  $M_{\text{BH}}$  versus  $M_q$  relation for QCCs (right). The  $M_{\text{BH}}$  is calculated using Equation 8. The yellow bands show the predicted  $M_{\text{BH}}-M_*$  relation (Equation 10) and its one- $\Delta$  uncertainty based on the best-fitting of the QGSR. The color-coded symbols and lines show the observational data (BH2 sample) with dynamically measured black hole masses and their best-fittings, taken from Graham & Sahu (2023). The red circles are elliptical galaxies, pink triangles are ES/S0 galaxies, and blue squares are spiral galaxies. The left panel show  $M_{\text{BH}}$  versus  $M_*$  while the right panel show  $M_{\text{BH}}$  versus  $M_{\text{sph}}$ , where  $M_{\text{sph}}$  is the mass of the spheroid component in a galaxy, derived using the decomposition technique. The purple/red/pink/blue lines show the best fitting for early-type (elliptical+ES/S0), elliptical, ES/S0 and spiral galaxies, respectively. We convert their Kroupa (Kroupa 2002) IMF to our Salpeter (Salpeter 1955) IMF by adding 0.30 dex in the stellar mass (see table 2 in Bernardi et al. (2010)).

given by Equation 5 with Equation 8 to obtain

$$M_{\text{BH}} = \gamma 10^{-\beta/\alpha} \sigma_{\text{in}}^{2+1/\alpha} = \gamma 10^{-\beta/\alpha} \sigma_{\text{in}}^{\alpha_{\text{MS}}}, \quad (9)$$

and

$$M_{\text{BH}} = \gamma 10^{2\beta} M_*^{1+2\alpha} = \gamma 10^{2\beta} M_*^{\alpha_{\text{MM}}}, \quad (10)$$

where  $\alpha = 0.30$  and  $\beta = -1.02$ , as obtained in Equation 5 (see Table 1). As a simple model, we assume that  $\gamma$  is a constant. In this case, we have only one model parameter, and we use the data of  $M_{\text{BH}}$  and velocity dispersion presented in Saglia et al. (2016) (hereafter the BH1 sample) for this purpose. The sample consists of 96 galaxies and we use all of them to obtain a best estimate for  $\gamma$ . This gives  $\gamma = 2.87 \times 10^{-8}$ , which completely specifies the two scaling relations given by Equations 9 and 10.

### 5.2. The validity of the model

With the value of  $\gamma$  calibrated, Equation 8 can be used to predict  $M_{\text{BH}}$  for each FQG and QCC. For QCCs, we use the mass within  $R_{\text{q}}$ , i.e.  $M_{\text{q}}$  (see Section 2.3) as  $M_*$ . The predicted  $M_{\text{BH}}$  versus  $\sigma_{\text{in}}$  relations for FQGs and QCCs are shown, respectively, as black circles in the left and right panels of Figure 18, together with Equation 9 (the yellow band in each panel). For comparison, the  $M_{\text{BH}}$  versus  $\sigma$  for galaxies in the BH1 sample (Saglia et al. 2016) are shown as red circles together with its best-fitting to a power-law relation between  $M_{\text{BH}}$  and  $\sigma_{\text{in}}$  (red lines). As one can see, the predicted  $M_{\text{BH}}$  is tightly correlated with  $\sigma_{\text{in}}$  for both FQGs and QCCs, and both populations follow the same trend described by Equation 9. Our model prediction also follows closely the trend defined by the BH1 sample. This is not trivial, as the host galaxies of QCCs are PQGs, which are morphologically different from FQGs, and consistent with the assertion that galaxies of different morphological types follow a similar  $M_{\text{BH}}-\sigma_{\text{in}}$  relation (e.g. Kormendy & Ho 2013). The slope of our  $M_{\text{BH}}-\sigma_{\text{in}}$  relation can be obtained directly from the QGSR. Using Equation 9, we obtain  $\alpha_{\text{MS}} = 2 + 1/\alpha = 5.39$ , in good agreement with the slope,  $5.25 \pm 0.27$ , obtained from the BH1 sample (Saglia et al. 2016).

Note that Saglia et al. (2016) adopted the effective velocity dispersion,  $\sigma_e$ , defined as the luminosity-weighted mean value of  $\sqrt{V^2(r) + \sigma^2(r)}$  within  $1R_e$ , with  $V(r)$  and  $\sigma(r)$  being the line-of-sight velocity and velocity dispersion, respectively. This is different from our  $\sigma_{\text{in}}$ . Our test shows that the  $\sigma_{\text{in}}-\sigma_e$  relations for FQGs and QCCs have very small scatter and lie closely to the 1:1 relation. It is consistent with the fact that these objects are hot systems, i.e. dispersion-dominated, and their dispersion profiles are flat. In fact, Saglia et al. (2016) also found that the dispersion is almost independent of radius. We thus anticipate that our results remain unchanged even if  $\sigma_e$  is used in Figure 18.

In Figure 19, we present the predicted  $M_{\text{BH}}-M_*$  ( $M_{\text{q}}$ ) relation for FQGs (QCCs), together with Equation 10 for reference. The two masses are tightly correlated, and both FQGs and QCCs follow the a similar relation that matches Equation 10. Saglia et al. (2016) did not provide stellar mass for galaxies in the BH1 sample. We thus compare our prediction with the black hole sample of Graham & Sahu (2023) (hereafter the BH2 sample)

that provides stellar mass of host galaxies. Interestingly, our FQGs follow closely early-type galaxies (ellipticals and ES/S0; left panel of Figure 19) in BH2. Graham & Sahu (2023) performed a linear regression for early-type galaxies and found a slope of  $1.59 \pm 0.11$ , which is shown as the purple line in the left panel. The slope of our prediction is  $\alpha_{\text{MM}} = 1 + 2\alpha = 1.59$  (Equation 10). Graham & Sahu (2023) also provided fitting results for ellipticals and ES/S0, separately (the red and pink lines in Figure 19). As one can see, the two lines are consistent with our prediction at the high- and low-mass ends, respectively. The discrepancy between the BH2 spiral galaxies (blue squares and line) and our FQGs is very large, as is expected because spiral galaxies are usually star-forming and our model only applies to quenched objects.

Graham & Sahu (2023) also provided the mass of the spheroid component ( $M_{\text{sph}}$ ) for each galaxy. The spheroid component represents an elliptical or the bulge of a spiral. It is thus interesting to compare results of our QCCs with those of spheroids, and the comparison is shown in the right panel of Figure 19. Our QCCs follow closely elliptical galaxies (red circles and line) in the BH2 sample. However, the results for bulges of ES/S0 galaxies (pink triangles and line) are very different. Graham & Sahu (2023) also found a significant offset in the  $M_{\text{BH}}-M_{\text{sph}}$  relation between ellipticals and bulges (see also Figure 19). At given  $M_{\text{BH}}$ , the bulge mass is about 0.5 dex smaller than that of the QCCs. Recently, Zhu et al. (2022b) decomposed stellar components of two nearby early-type galaxies using dynamical information obtained from IFU spectroscopy. In addition to bulges, they found another dynamically hot component within  $2R_e$  of the galaxies, and referred to it as a dynamically hot inner stellar halo (DHISH). The mass of DHISH is about 30% of the total stellar mass. Similar components can also be found in simulated galaxies (Zhu et al. 2022a), with the mass fraction ranging from several to more than fifty percents. The tension between our prediction and the observed  $M_{\text{BH}}-M_{\text{sph}}$  relation can thus be alleviated by including DHISH.

To quantify the performance of our model, we adopt two  $\chi^2$  parameters to measure the differences between the model prediction and observational data. For BH1 the  $\chi^2$  is:

$$\chi_1^2 = \frac{1}{N_1} \sum_{i=1}^{N_1} \frac{(\log M_{\text{BH}}(\sigma_i) - \log M_{\text{BH1},i})^2}{e_{M_{\text{BH1},i}}^2 + \alpha_{\text{MS}}^2 e_{\sigma_i}^2 + \frac{1}{\alpha^2} \Delta_{\text{q}}^2}, \quad (11)$$

where  $M_{\text{BH1},i}$  and  $e_{M_{\text{BH1},i}}$  are the measurement of  $M_{\text{BH}}$  and its uncertainty for the  $i$ th galaxy in BH1,  $\sigma_i$  and  $e_{\sigma_i}$  are the measurement of the velocity dispersion and its uncertainty. The data are taken from Saglia et al. (2016), and the sample size is  $N_1 = 96$ . The mass  $M_{\text{BH}}(\sigma_i)$  in the above equation is the prediction of Equation 9 for the  $i$ th galaxy. For BH2, the  $\chi^2$  is defined as

$$\chi_2^2 = \frac{1}{N_2} \sum_{i=1}^{N_2} \frac{(\log M_{\text{BH}}(M_{*,i}) - \log M_{\text{BH2},i})^2}{e_{M_{\text{BH2},i}}^2 + \alpha_{\text{MM}}^2 e_{M_{*,i}}^2 + 4\Delta_{\text{q}}^2}, \quad (12)$$

which is the same as Equation 11, except that it is for the  $N_2 = 67$  elliptical and ES/S0 galaxies in the BH2 sample, with data taken from Graham & Sahu (2023). The black hole mass,  $M_{\text{BH}}(M_{*,i})$ , is predicted by Equation 10. Note

that any covariance in the measurements are ignored, but the intrinsic scatter of the QGSR is included. We obtain  $\chi_1^2 = 1.80$  and  $\chi_2^2 = 2.17$ , indicating that our model predictions are consistent with the observational data.

### 5.3. Implications of the model

The fact that our simple model based on scaling relations of FQGs and QCCs can reproduce the observed black hole mass suggests that quenching of star formation and the growth of SMBHs are closely linked, and both are related to the dynamically hot stellar component. In our simple model, the parameter  $\gamma$  is assumed to be constant, and its value is well constrained by observational data. Since  $\gamma$  is a combination of processes specified by  $a$ ,  $f_{\text{gas}}$ ,  $\epsilon$  and  $f_{\text{cp}}$  (Equation 8), we may use the constrained value to examine its implications for the related processes. The parameter  $a$  is related to the shape and dynamical status of a galaxy. For a virialized, uniform sphere, we have  $a^2 \approx 6$ . The value of  $f_{\text{cp}}$  is uncertain. For an AGN in the high-accretion phase where radiation is the dominating feedback channel,  $f_{\text{cp}}$  is usually assumed to be about 0.05 (e.g. Springel et al. 2005; Hopkins et al. 2006). However, the value could be much lower according to the observational studies (He et al. 2019, 2022). Assuming that  $\epsilon = 0.1$  and  $a^2 = 6$ , we obtain  $f_{\text{gas}} = 4.8(f_{\text{cp}}/0.05)$ . Thus, the average amount of gas that can be prevented from forming stars can be significant. Note that  $f_{\text{gas}}$  may vary from one system to another. At a given  $M_*$ , a black hole in a gas-rich system has to release more energy to quench the system than that in a gas-poor system, which leads to more growth in the mass of the black hole. Therefore, the final  $M_{\text{BH}}$  is expected to depend on the gas richness before quenching. This suggests that the intrinsic scatter in BHSRs should be larger than the prediction of our simple model that does not include the scatters in model parameters. It is consistent with that both  $\chi_1^2$  and  $\chi_2^2$  are larger than one.

At low  $\sigma_{\text{in}}$  end, the predicted  $M_{\text{BH}}-\sigma_{\text{in}}$  relation systematically deviates from the observational results. These black holes usually reside in low-mass galaxies. As shown in Figure 9, low-mass FQGs usually have larger gradients in their  $\sigma$  profiles. The gas in the outskirts can thus escape more easily, and the value of  $a$  is lower, than the gas in the outskirts of more massive galaxies. This can lower the predicted  $M_{\text{BH}}$  for low-mass galaxies. Furthermore, stellar feedback may play a more important role in low-mass galaxies, which can reduce the accretion rate of black holes and their mass growth, as suggested by Hopkins et al. (2022).

The difference between our QCCs and bugles (Figure 19) suggests that the galaxy-black hole relation defined by stellar components is related to the growth of the central black hole. Zhu et al. (2022a) analyzed the DHISH components in simulated galaxies and found that they are directly produced by galaxy mergers. These mergers are expected to trigger strong AGNs and cause significant growth in the mass of the SMBH. This suggests that the DHISH should be an important part of the galaxy-black hole relation, and is needed to explain the difference in the  $M_{\text{sph}}-M_{\text{BH}}$  relation between elliptical galaxies and bulges found by Graham & Sahu (2023).

## 6. SUMMARY

In this paper, we use MaNGA galaxies to investigate the relationships among galaxy dynamical status, galaxy quenching, supermassive black hole mass, and the co-evolution of galaxy dynamical and quenching properties. The spatially resolved dynamical property, as represented by stellar velocity dispersion, and stellar population property represented by D4000 make it possible to establish the connection in such a way as to make physical interpretations more straightforward. We only use central galaxies to avoid contamination by environmental effects. Our main results are summarized below.

Different from most of previous studies, we use the fraction of quenched spaxels to classify galaxies into three classes, fully quenched (FQGs), partially quenched (PQGs) and fully star-forming galaxies (FSGs). We find that most FQGs have very weak star formation activity, with  $\log \text{sSFR} < -12$ , while FSGs have strong star formation, with  $\log \text{sSFR} > -10.6$ . PQGs have quenched fractions between 5% and 95% and  $\log \text{sSFR}$  between those of FSGs and FQGs (Figure 5). We also identify quenched central cores (QCCs) that have quenched fraction similar to FQGs.

We define a scaling relation of dynamical hotness (SRDH) using the  $M_*-\sigma_{\text{hot}}$  relation of dynamically hot galaxies (Equation 4). We use the difference between the observed velocity dispersion of a galaxy and  $\sigma_{\text{hot}}(M_*)$  given by the SRDH for its stellar mass to describe its dynamical hotness. The Two- $\sigma$  diagram, which plots the scaled inner velocity dispersion ( $\log(\sigma_{\text{in}}/\sigma_{\text{hot}})$ ) versus the scaled velocity dispersion in the outer part ( $\log(\sigma_{\text{out}}/\sigma_{\text{hot}})$ ), Figure 10), is used to distinguish between centrally and totally hot galaxies. We find that both FQGs and QCCs occupy a small region around (0,-0.05) in this diagram, demonstrating that FQGs and QCCs are dynamically hot over their entire bodies. In contrast, most PQGs and FSGs are located below the SRDH (Figure 4), indicating that they are dynamically colder. PQGs have a very broad distribution in  $\log(\sigma_{\text{out}}/\sigma_{\text{hot}})$  and form an extended vertical band in the Two- $\sigma$  diagram (Figure 10). This suggests that PQGs are dynamically hot in central regions but dynamically cold in outskirts. FSGs have an even broader distribution in dynamical state: they can not only reside in the vertical band defined by PQGs, but also in a horizontal sequence where a galaxy is cold both in the inner and outer regions.

The distribution of galaxies in the Two- $\sigma$  diagram shows clear evolutionary connections and transitions of galaxy properties, such as morphology, star formation and AGN activity (Figure 17). We define a horizontal sequence ( $\log(\sigma_{\text{out}}/\sigma_{\text{hot}}) < -0.5$ ), in which galaxies remain dynamically cold in outer regions, and a vertical sequence ( $\log(\sigma_{\text{in}}/\sigma_{\text{hot}}) > -0.3$ ), in which galaxies are centrally hot (Figure 10), to follow the evolution of the galaxy population. On the horizontal sequence, centrally cold galaxies are dominated by star-forming disks, and grow via star formation. The central velocity dispersion increases gradually while the outskirts remains cold. AGN activities are rare and so no significant quenching of star formation occurs. When the central dispersion of a galaxy reaches about half of the value given by the SRDH according to its mass, the galaxy becomes more concentrated and morphologically more diverse. Optical AGNs then appear frequently and galaxies can be quenched in

central regions, leading to the emergence of QCCs and PQGs. As the outskirts of cold disks are heated up gradually, galaxies move upwards along the vertical sequence, eventually reaching the top of the vertical sequence and becoming dynamically hot. Their star formation can be quenched if strong AGNs are triggered during the process. For a hot massive galaxy, accretion of hot gas may ignite radio AGN, which can heat the surrounding gas and keep the galaxy quenched. All these processes seem to lead to two transitions in the  $s\text{SFR}-\sigma_{\text{in}}$  and  $s\text{SFR}-\sigma_{\text{out}}$  diagrams when galaxies move along the horizontal and vertical sequences (Figure 14 and 16).

Our results suggest that both secular and rapid processes can drive the evolution and change of galaxy dynamical status (Figure 10). We find that barred galaxies tend to lie exactly on the vertical sequence, consistent with the fact that bars can redistribute gas and stars and drive the growth of central concentration. Galaxies with large central velocity dispersion and dynamically hot FSGs both tend to exhibit signatures of strong interactions and mergers. This indicates that these processes can change the dynamical state of a galaxy very quickly. We find that optically selected AGNs tend to lie on the vertical sequence where quenching starts and that radio galaxies can only be found in dynamically hot galaxies where the evolution in the dynamical state of a galaxy cannot proceed further. These results suggest that AGNs are connected to the change of the dynamical status and quenching of galaxies, consistent with the

hypothesis that AGN feedback plays an important role in quenching star formation.

We construct a simple model to link the energy released by AGNs and the energy required to get rid of star-forming gas. Since our observational results show that only dynamically hot systems can be quenched, the model applies only to quenched and dynamically hot systems, such as FQGs and QCCs. We use the model to predict the mass of SMBHs,  $M_{\text{BH}}$ , and find the predicted  $M_{\text{BH}}-\sigma_{\text{in}}$  and  $M_{\text{BH}}-M_*$  relations are in good agreement with observational data (Figure 18 and 19). All these show that the formation of dynamically hot systems, the growth of SMBHs and quenching of star formation are closely connected with each other.

#### ACKNOWLEDGEMENTS

We thank Kai Wang and Huiling Liu for helpful discussions. We thank the referee for useful suggestions. This work is supported by the National Key R&D Program of China (grant No. 2018YFA0404503), the National Natural Science Foundation of China (NSFC, Nos. 12192224, 11733004 and 11890693), CAS Project for Young Scientists in Basic Research, Grant No. YSBR-062, and the Fundamental Research Funds for the Central Universities. We acknowledge the science research grants from the China Manned Space Project with No. CMS-CSST-2021-A03. The authors gratefully acknowledge the support of Cyrus Chun Ying Tang Foundations. The work is also supported by the Supercomputer Center of University of Science and Technology of China.

#### REFERENCES

- Abdurro'uf, Accetta, K., Aerts, C., et al. 2022, *ApJS*, 259, 35  
 Aller, M. C., & Richstone, D. O. 2007, *ApJ*, 665, 120  
 Aquino-Ortiz, E., Valenzuela, O., Sánchez, S. F., et al. 2018, *MNRAS*, 479, 2133  
 Baldry, I. K., Glazebrook, K., Brinkmann, J., et al. 2004, *ApJ*, 600, 681  
 Barro, G., Faber, S. M., Koo, D. C., et al. 2017, *ApJ*, 840, 47  
 Bender, R., Burstein, D., & Faber, S. M. 1992, *ApJ*, 399, 462  
 Bernardi, M., Shankar, F., Hyde, J. B., et al. 2010, *MNRAS*, 404, 2087  
 Best, P. N., & Heckman, T. M. 2012, *MNRAS*, 421, 1569  
 Blanton, M. R., Kazin, E., Muna, D., Weaver, B. A., & Price-Whelan, A. 2011, *AJ*, 142, 31  
 Blanton, M. R., Schlegel, D. J., Strauss, M. A., et al. 2005, *AJ*, 129, 2562  
 Bluck, A. F. L., Maiolino, R., Brownson, S., et al. 2022, *A&A*, 659, A160  
 Bluck, A. F. L., Maiolino, R., Sánchez, S. F., et al. 2020a, *MNRAS*, 492, 96  
 Bluck, A. F. L., Mendel, J. T., Ellison, S. L., et al. 2014, *MNRAS*, 441, 599  
 —. 2016, *MNRAS*, 462, 2559  
 Bluck, A. F. L., Maiolino, R., Piotrowska, J. M., et al. 2020b, *MNRAS*, 499, 230  
 Bogdán, Á., Lovisari, L., Volonteri, M., & Dubois, Y. 2018, *ApJ*, 852, 131  
 Boselli, A., Fossati, M., & Sun, M. 2022, *A&A Rev.*, 30, 3  
 Bower, R. G., Benson, A. J., Malbon, R., et al. 2006, *MNRAS*, 370, 645  
 Brinchmann, J., Charlot, S., White, S. D. M., et al. 2004, *MNRAS*, 351, 1151  
 Brook, C. B., Stinson, G. S., Gibson, B. K., et al. 2012, *MNRAS*, 426, 690  
 Brownson, S., Bluck, A. F. L., Maiolino, R., & Jones, G. C. 2022, *MNRAS*, 511, 1913  
 Bruzual A., G. 1983, *ApJ*, 273, 105  
 Bundy, K., Bershady, M. A., Law, D. R., et al. 2015, *ApJ*, 798, 7  
 Cappellari, M. 2016, *ARA&A*, 54, 597  
 Cardelli, J. A., Clayton, G. C., & Mathis, J. S. 1989, *ApJ*, 345, 245  
 Chen, G., Zhang, H.-X., Kong, X., et al. 2020a, *ApJ*, 895, 146  
 Chen, Z., Faber, S. M., Koo, D. C., et al. 2020b, *ApJ*, 897, 102  
 Cheung, E., Faber, S. M., Koo, D. C., et al. 2012, *ApJ*, 760, 131  
 Croton, D. J., Springel, V., White, S. D. M., et al. 2006, *MNRAS*, 365, 11  
 Davé, R., Anglés-Alcázar, D., Narayanan, D., et al. 2019, *MNRAS*, 486, 2827  
 Di Matteo, T., Springel, V., & Hernquist, L. 2005, *Nature*, 433, 604  
 Du, M., Ho, L. C., Debattista, V. P., et al. 2020, *ApJ*, 895, 139  
 Dubois, Y., Peirani, S., Pichon, C., et al. 2016, *MNRAS*, 463, 3948  
 Ellison, S. L., Sánchez, S. F., Ibarra-Medel, H., et al. 2018, *MNRAS*, 474, 2039  
 Fabello, S., Catinella, B., Giovanelli, R., et al. 2011, *MNRAS*, 411, 993  
 Faber, S. M., & Jackson, R. E. 1976, *ApJ*, 204, 668  
 Fabian, A. C. 1999, *MNRAS*, 308, L39  
 —. 2012, *ARA&A*, 50, 455  
 Fang, J. J., Faber, S. M., Koo, D. C., & Dekel, A. 2013, *ApJ*, 776, 63  
 Feoli, A., & Mele, D. 2005, *International Journal of Modern Physics D*, 14, 1861  
 Ferrarese, L., & Merritt, D. 2000, *ApJ*, 539, L9  
 Foreman-Mackey, D., Hogg, D. W., Lang, D., & Goodman, J. 2013, *PASP*, 125, 306  
 Franx, M., van Dokkum, P. G., Förster Schreiber, N. M., et al. 2008, *ApJ*, 688, 770  
 Gallazzi, A., Charlot, S., Brinchmann, J., & White, S. D. M. 2006, *MNRAS*, 370, 1106  
 Gebhardt, K., Bender, R., Bower, G., et al. 2000, *ApJ*, 539, L13  
 Goodman, J., & Weare, J. 2010, *Communications in Applied Mathematics and Computational Science*, 5, 65  
 Gorgas, J., Cardiel, N., Pedraz, S., & González, J. J. 1999, *A&AS*, 139, 29  
 Graham, A. W. 2008, *ApJ*, 680, 143  
 Graham, A. W., & Guzmán, R. 2003, *AJ*, 125, 2936  
 Graham, A. W., & Sahu, N. 2023, *MNRAS*, 518, 2177  
 Hart, R. E., Bamford, S. P., Willett, K. W., et al. 2016, *MNRAS*, 461, 3663  
 He, Z., Wang, T., Liu, G., et al. 2019, *Nature Astronomy*, 3, 265  
 He, Z., Liu, G., Wang, T., et al. 2022, *Science Advances*, 8, eabk3291  
 Heckman, T. M., & Best, P. N. 2014, *ARA&A*, 52, 589  
 Hopkins, P. F., Hernquist, L., Cox, T. J., et al. 2006, *ApJS*, 163, 1

- Hopkins, P. F., Hernquist, L., Cox, T. J., Robertson, B., & Krause, E. 2007a, *ApJ*, 669, 45  
— 2007b, *ApJ*, 669, 67
- Hopkins, P. F., & Quataert, E. 2011, *MNRAS*, 415, 1027
- Hopkins, P. F., Wellons, S., Anglés-Alcázar, D., Faucher-Giguère, C.-A., & Grudić, M. Y. 2022, *MNRAS*, 510, 630
- Ibata, R. A., Lewis, G. F., McConnachie, A. W., et al. 2014, *ApJ*, 780, 128
- Ilbert, O., McCracken, H. J., Le Fèvre, O., et al. 2013, *A&A*, 556, A55
- Kauffmann, G., Heckman, T. M., White, S. D. M., et al. 2003, *MNRAS*, 341, 33
- Kennicutt, Robert C., J. 1998, *ARA&A*, 36, 189
- Kewley, L. J., Dopita, M. A., Sutherland, R. S., Heisler, C. A., & Trevena, J. 2001, *ApJ*, 556, 121
- Kormendy, J., & Ho, L. C. 2013, *ARA&A*, 51, 511
- Kormendy, J., & Kennicutt, Robert C., J. 2004, *ARA&A*, 42, 603
- Kroupa, P. 2002, *Science*, 295, 82
- Li, C., Wang, E., Lin, L., et al. 2015, *ApJ*, 804, 125
- Li, P., Wang, H., Mo, H. J., Wang, E., & Hong, H. 2020, *ApJ*, 902, 75
- Magorrian, J., Tremaine, S., Richstone, D., et al. 1998, *AJ*, 115, 2285
- Mancini, L., & Feoli, A. 2012, *A&A*, 537, A48
- Marconi, A., Risaliti, G., Gilli, R., et al. 2004, *MNRAS*, 351, 169
- Mo, H., van den Bosch, F. C., & White, S. 2010, *Galaxy Formation and Evolution*
- Muzzin, A., Marchesini, D., Stefanon, M., et al. 2013, *ApJ*, 777, 18
- Oh, S., Colless, M., Barsanti, S., et al. 2020, *MNRAS*, 495, 4638
- Peng, Y.-j., Lilly, S. J., Kovač, K., et al. 2010, *ApJ*, 721, 193
- Pillepich, A., Springel, V., Nelson, D., et al. 2018, *MNRAS*, 473, 4077
- Piotrowska, J. M., Bluck, A. F. L., Maiolino, R., & Peng, Y. 2022, *MNRAS*, 512, 1052
- Posti, L., Fraternali, F., & Marasco, A. 2019, *A&A*, 626, A56
- Saglia, R. P., Opitsch, M., Erwin, P., et al. 2016, *ApJ*, 818, 47
- Sahu, N., Graham, A. W., & Davis, B. L. 2019, *ApJ*, 876, 155  
— 2020, *ApJ*, 903, 97
- Salpeter, E. E. 1955, *ApJ*, 121, 161
- Sánchez, S. F., Pérez, E., Sánchez-Blázquez, P., et al. 2016a, *RMxAA*, 52, 21  
— 2016b, *RMxAA*, 52, 171
- Sánchez, S. F., Barrera-Ballesteros, J. K., Lacerda, E., et al. 2022, *ApJS*, 262, 36
- Schaye, J., Crain, R. A., Bower, R. G., et al. 2015, *MNRAS*, 446, 521
- Silk, J., & Rees, M. J. 1998, *A&A*, 331, L1
- Soker, N., & Meiron, Y. 2011, *MNRAS*, 411, 1803
- Sotillo-Ramos, D., Pillepich, A., Donnari, M., et al. 2022, *MNRAS*, 516, 5404
- Springel, V., Di Matteo, T., & Hernquist, L. 2005, *MNRAS*, 361, 776
- Straatman, C. M. S., Labbé, I., Spitler, L. R., et al. 2014, *ApJ*, 783, L14
- Strateva, I., Ivezić, Ž., Knapp, G. R., et al. 2001, *AJ*, 122, 1861
- Terrazas, B. A., Bell, E. F., Pillepich, A., et al. 2020, *MNRAS*, 493, 1888
- Wagner, A. Y., Umemura, M., & Bicknell, G. V. 2013, *ApJ*, 763, L18
- Wake, D. A., van Dokkum, P. G., & Franx, M. 2012, *ApJ*, 751, L44
- Wake, D. A., Bundy, K., Diamond-Stanic, A. M., et al. 2017, *AJ*, 154, 86
- Wang, E., Li, C., Xiao, T., et al. 2018a, *ApJ*, 856, 137
- Wang, E., Wang, H., Mo, H., et al. 2018b, *ApJ*, 860, 102
- Wang, H., Mo, H. J., Chen, S., et al. 2018c, *ApJ*, 852, 31
- Wechsler, R. H., & Tinker, J. L. 2018, *ARA&A*, 56, 435
- Willett, K. W., Lintott, C. J., Bamford, S. P., et al. 2013, *MNRAS*, 435, 2835
- Woo, J., Dekel, A., Faber, S. M., & Koo, D. C. 2015, *MNRAS*, 448, 237
- Yan, R., Chen, Y., Lazarz, D., et al. 2019, *ApJ*, 883, 175
- Yang, X., Mo, H. J., van den Bosch, F. C., et al. 2007, *ApJ*, 671, 153
- Zehavi, I., Zheng, Z., Weinberg, D. H., et al. 2011, *ApJ*, 736, 59
- Zhang, Z., Wang, H., Luo, W., et al. 2022, *A&A*, 663, A85  
— 2021, *A&A*, 650, A155
- Zhu, L., van den Bosch, R., van de Ven, G., et al. 2018, *MNRAS*, 473, 3000
- Zhu, L., Pillepich, A., van de Ven, G., et al. 2022a, *A&A*, 660, A20
- Zhu, L., van de Ven, G., Leaman, R., et al. 2022b, *A&A*, 664, A115
- Zinger, E., Pillepich, A., Nelson, D., et al. 2020, *MNRAS*, 499, 768